Multibeam electron optical system - Neighbours matter

Adriaans, Martijn J.

Award date:
2020

Multibeam Electron Optical System – Neighbors matter

Martijn Adriaans, 2020

Graduation thesis at Eindhoven University of Technology

Group: Coherence and Quantum Technology, in collaboration with Thermo Fisher Scientific

TU/e supervisor: Dr. Peter Mutsaers

Thermo Fisher supervisor: Dr. Ali Mohammadi-Gheidari

Report number: CQT 2020-20

Abstract

In this thesis, an important step is made towards improving the electron optical performance of the multibeam source designed for a multibeam scanning electron microscope, accounting for its better further commercialization for high throughput electron beam imaging and lithography techniques. The array of images produced by the multibeam source have been suffering from an unwanted octupole aberration introduced by the orthogonally distributed neighbor aperture lenses at the aperture lens array. This thesis focuses on the evaluation of this octupole defect systematically and proposes methods for its elimination and achieves this result in several steps. First, multiple computational strategies for characterization of the octupole field are discussed. It is concluded that the most accurate method to calculate the octupole aberration coefficient is through a so called “ray tracing and fitting”. In this method the electrons are traced through the numerically calculated 3D electrostatic field and then by mapping the initial particle positions and momenta to their positions and momenta on the image plane, octupole aberration coefficient is calculated. Octupole cancellation is done by engineering variations of the ALA micro-aperture shape, which include adding aperture walls, (blind hole) indentations, changing the aperture shapes to a semicircular or rounded square aperture shape and a hexagonally distributed aperture pattern with aperture walls, where each variation is characterized by an optimization parameter. This parameter is optimized for each geometry, leading to a minimized octupole aberration coefficient for each case. Then using the (FW_{50}) sizes of both the central beamlets and an off-axis beamlet, the off-axial aberration influences, and the parameter sensitivity, different correcting methods are compared. Though the largest off-axial spot (in FW_{50}) is found for correction by indentations, the off-axial influences might be controlled through further investigation. The largest central spot is found for semicircular holes, which may be due to the introduction of higher order aberrations. Moreover, the higher precision required for the construction of semicircular holes, makes this a less viable option. The aperture walls are concluded to eliminate the octupole aberration while keeping the influence of other aberrations to a minimum.

Contents

1 An introduction to the multibeam electron optical system

In a conventional light microscope, as shown schematically in Figure 1, the optical elements in the optical system bend the paths of the photons emerging from a light source to illuminate the sample and then using another set of lenses, the transmitted light beam is focused in the image plane to form an image of the sample. The interaction of the light beam with the sample causes absorption and scattering of photons in the bundle leading to a difference in intensity at different points in the image plane, called contrast. The optical resolving power and thus the resolution of the image depend on several optical limiting factors in the optical system but also on the sample itself and the nature of photon sample interaction. The ultimate resolution is, however, limited by the wavelength of the photons. Due to the wave nature of light, diffraction dictates the ultimate resolving power of the microscope. The best achievable resolution with a traditional light microscope using the shortest observable wavelength of 400 nm, is limited to similarly sized details. In order to improve the resolution of light -based imaging and pattering systems, there have been tremendous efforts dedicated to this subject in the past couple of decades. The most straight forward solution is to use “light” with a shorter wavelength from the EM spectrum. One example being, the newest EUV-based lithography machines produced by ASML use an extreme ultraviolet source of 13.5 nm to fabricate sub-20 nm features and patterns to be used in semiconductor chip industry [1].

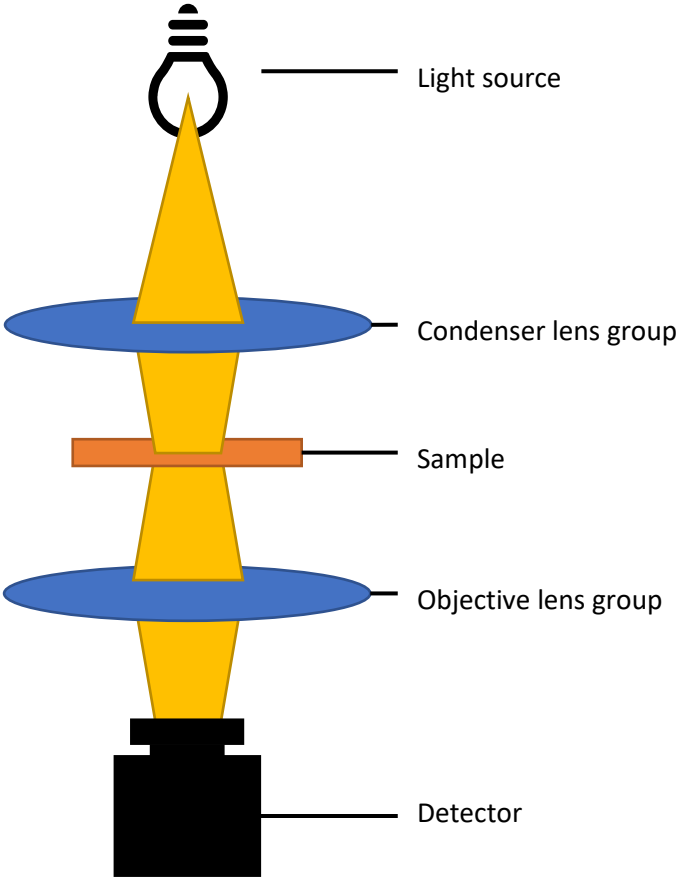

Figure 1: schematic representation of light microscope. In a TEM, the idea of the setup is essentially the same, but here the light source is replaced by an electron source, and lens groups are replaced by electromagnetic optical elements such as coils / deflectors etc.

An alternative technology, surpassing the diffraction limit of the light optical systems, is used in electron optical systems, or in general "Charged Particle Optical" systems. Unlike light optical systems, the ultimate resolution of charged particle optical systems is not determined by the wavelength of the electrons because the electron wavelength inversely scales with the acceleration voltage of the electrons and can be made extremely small by accelerating them to high energies. In fact, this was the main driving force behind the development of the very first electron microscope known as TEM (Transmission Electron Microscope) by E. Ruska and others [2]. Its design was somewhat an exact copy of light microscope in which the light source is replaced with electron source and light lenses are replaced with electromagnetic lenses. In a typical TEM, electrons accelerated to only 100 keV will have a wavelength of only 0.0037 nm [3]. Nowadays powerful TEM's, equipped with aberration correctors and hight brightness electron source can produce images with 0.05 nm resolution at typical acceleration voltage of 300kV [4]. Immediately after the introduction of the TEM's, another class of electron microscope, a Scanning Electron Microscope (SEM), emerged [5]. In an SEM, electrons are accelerated and focused using electromagnetic lenses down to a small point, an electron probe, on the surface of a sample. This focused probe is then scanned across the surface of the sample, by the deflection/scanning unit, pixel by pixel in order to produce an image of the surface topography of the sample or to write a pattern on it. The current SEM design is schematically depicted in Figure 2 (be aware to imagine a standard SEM with only a single central beam in the figure).

State-of-the-art high-resolution SEMs can reach a resolution below 1 nm with a typical beam current of about 50 pA. With this typical probe current, making a sub-1 nm resolution image of a sample, or scanning roughly 10^6 pixels, is typically a matter of a second [6]. When used for patterning, this can take an order of magnitude longer. In short, when the sample surface scanning area is limited to μm^2, current SEM is fast enough to produce images in a matter of seconds, minutes, or an hour depending on the size of the sample. This is not, however, true when imaging or patterning a larger area sample. Think about imaging/patterning the whole surface of a 350 mm Si-wafer used in semiconductor chip industry. Using current SEM, it takes years to image /pattern all the features required for a single functioning chip in a full wafer. In order to increase the throughput, a higher probe current is required. Unfortunately, the probe current cannot be simply increased. Let's see why is this true. The probe current in an SEM can be written as [7]:

$$I = B_r \frac{\pi^2}{4} \left(d_{geo}\right)^2 \alpha^2 V, \qquad (1)$$

Where B_r is the reduced brightness of the electron source, $d_{geo} = M d_v$ is the geometrical source image at the sample, M is the total magnification of the electron lenses, d_v is the virtual source size, α is the half opening angle of the probe and V is the acceleration voltage.

From equation (1) it is clear that the probe current is ultimately limited by the reduced brightness of the electron source for an optimized α with which the aberration contributions from the lenses are minimized. Moreover, increasing the beam current increases the coulomb repulsion between electrons which degrades the resolution.

Multi beam technology is a solution to the throughput problem of current SEM's. To this end, a Multi Beam Scanning Electron Microscope (MBSEM) has been designed and developed at the Delft University of Technology which delivers an array of 14x14 (196) focused beams onto the sample simultaneously [7]. Figure 2 shows the electron optical working principle of the MBSEM schematically. One of the essential parts of the MBSEM is the Multi Beam Source (MBS) which produces an array of beams for the rest of the electron optical column of the MBSEM. The MBS, depicted in Figure 3 is composed of the electron source unit, two macro-electrodes (E-1 and E-2) and an array of micro- apertures fabricated using MEMS techology. These micro-apertures play double roles: 1]- they split the solid emission cone of the electron source into an array of beams and 2]- in combination with the electron source unit and two macro-electrodes produces aperture lens array (ALA) to focus different beams to the MBS image plane. The focused array of images of the source in the MBS image plane are consequently accelerated and directed to the SEM optics column by the accelerator lens (ACC.) and further focused by the downstream electromagnetic lenses (C2, INT and HR/UHR) onto the surface of a sample. By positioning the common crossover of the multiple beams at the variable aperture (VA) , the beam current of all individual beams can be tuned by simply selecting different sizes of the VA. With the configuration explained above, the MBSEM produces 196 beams at the sample with 1 nm resolutions and a typical current per beam of about 50 pA, both comparable to the those of state-of-the-art high resolution (single) beam SEM. In this case, usually most of the current through the ALA is stopped by the VA. However, for very high current applications of around 1 nA per beam, the VA can no longer be a beam limiting aperture. As depicted in Figure 3, this means all the current through the ALA will contribute in the probe formation, which is indicated by the blue instead of the green bundle cross-section. That means the same micro-apertures at

the aperture array act also as a beam limiting apertures and the filling factor[1] of these apertures becomes 100%. Once this is the case, a remarkable octupole aberration appears in the probe, enlarging the probe size thus degrading the resolution remarkably. This octupole aberration is due to the influence of nearby apertures in the ALA that deviate the rotational symmetric field near every aperture hole.

This leads to the main questions of this thesis, being "how can we evaluate this octupole aberration correctly" in the first place and the following question is, "how can we eliminate it?" The thesis is organized as follows: Section 2 introduces the multipole problem in more detail, and then answers the question "which computational strategy works best here?". Then, in section 3, the numerical settings and other factors affecting the accuracy of the simulation are discussed. Then we may ask ourselves "how do we design the ALA such that the octupole is corrected?" To this end, different correction shapes are presented in section 4. In section 5, these correction methods are optimized and the differences are discussed. Further exploration of optical problems is discussed in section 6 and in section 7, a conclusion is drawn.

The original plan in the project was first numerically optimize the ALA such that the octupole is eliminated. Due to COVID-19, the accessibility to Thermo Fisher Scientific's premises was extremely limited and the production of the ALA itself was effectively put to a stop. Instead of pursuing this experimental verification of the shapes presented in section 5, it was decided that a (brief) comparison between older experiments and simulation here, should suffice to demonstrate the accuracy of the simulations. This is done as part of the discussion of the numerical accuracy in section 3.6.

[1]Here the filling factor is defined as the ratio of the current filling the micro-aperture at ALA and the current in the corresponding probe at the sample.

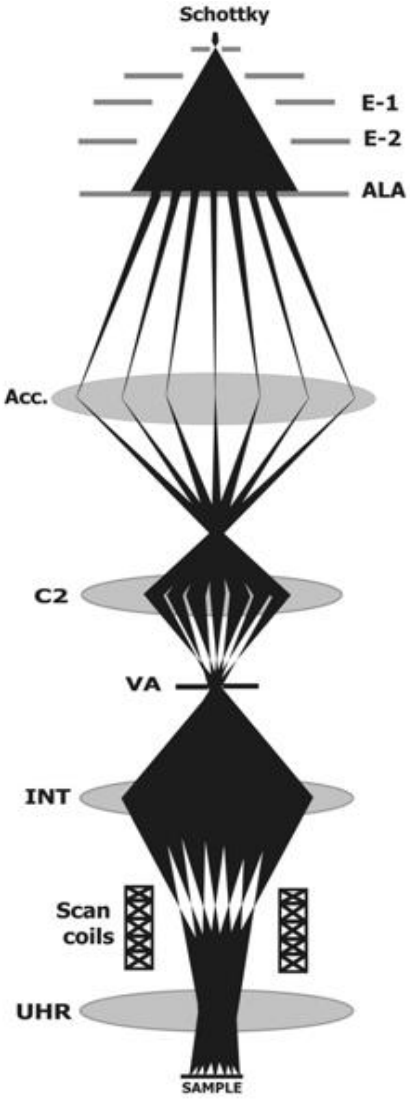

Figure 2: Schematic drawing of an SEM column where with only one central beam it depicts an standard (single) beam SEM and with all multiple beams simultaneously, it depicts a multibeam scanning electron microscope (MBSEM). The Schottky source and the first two electrostatic lenses (E-1 and E-2) together witht the aperture lens array (ALA) make up the multi beam source (MBS), which produces multiple beamlets. These are consequently accelerated by the accelerator lens (Acc.), and focused before the C2 lens to a common crossover, which is image by the C2 lens in another common crossover at the variable aperture (VA) plane. The VA controls the beam opening angle and beam current in a single aperture for all beamlets. The intermediate lens (INT) fosuses the common crossover of the VA to the "coma free plane" of the ultra high resolution (UHR) objective lens. This ensures that off-axial aberrations, caused partly by scanning the probe over the sample using the scan coils, are minimized. Finally, the ultra high resolution (UHR) objective lens focuses the beamlets on the sample. The image is taken from *[7]*.

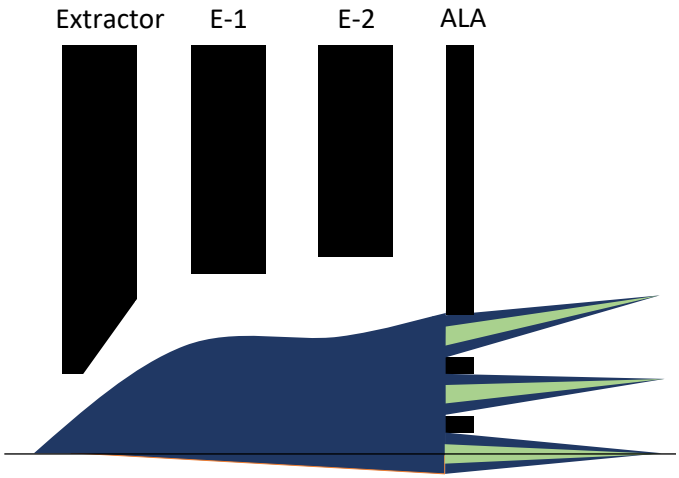

Figure 3: Schematically depicts the MBS. As the name suggests, the extractor extracts electrons from a Schottky electron source. The beam is then modified by a macro-electrostatic lens. The macro electrodes, E-1 and E-2 were originally designed as a single apertures, but as can be seen in Figure 21, both are now designed as a pair of apertures. The ALA makes an array of focused images of the electron source. The green part of the beam (for every beamlets) indicates the part of the beam being let through by the VA whereas the whole current of every beamlet (blue) is used for when there is no VA (filling factor of the micro-apertures being 100%). The diameter of these apertures and the pitch between them are typically one or a few tens of micrometers.

2 The octupole aberration of the ALA

As mentioned earlier, to obtain higher probe current, the variable aperture (VA) is removed from the MBSEM and every micro-aperture in the ALA is the only beam limiting aperture in the system. That is, the filling factors of the micro-apertures are 100%, whereas for a high resolution MBSEM, this was less than 5% (Figure 3). In this situation, the presence of many neighbor micro-aperture lenses in the ALA leads to an additional multipole effect in the individual beamlets. Due to many neighbor micro-aperture lenses, the electric fields around an aperture hole are not rotationally symmetric. This causes deflections of the electrons and leads to the octupole aberration, which will be introduced in section 2.1.

This effect has been observed experimentally previously using a slightly different setup where multiple array elements are involved [8], and more recently [9] for a design where the ALA is the only non-rotationally symmetric element. This effect is found to be a dominant aberration contribution enlarging the spot size of the beams at the MBS image plane. Figure 4b shows a simulated spot profile at the MBS image plane for an axial micro-aperture lens with neighbor micro-aperture lenses. Figure 4d shows the spot profile for the same micro-aperture lens when all neighbor aperture lenses are removed. The aberrations induced by the neighbor apertures enlarges the spot size by a factor of 2.7, measured in FW_{50} [2]. Judging from the rectangular aperture pattern around the central aperture, the aberrations that are induced are expected to be 4-fold symmetric. In Figure 4b it appears that the four-fold symmetric shape isn't very obvious in the focus plane but rather there is a large spread in the spot. To see the four-fold shape in the beam more pronounced, the spot profiles are also shown before and after the focus plane, for the same simulation. Figure 4a and Figure 4c show the same spot shown at Figure 4b at two different planes of under- and over-focus demonstrating clearly the octupole effect. From these two figures it appears that the start shape has "changed" the direction by 45 degrees. This means that only judging from the orientation of the star shaped spot or its size is not enough to determine the direction and strength of the octupole, which calls for an adequate fitting procedure. It should be noted that all simulations have been carried out using newly developed software BEM+GPT by Pulsar Physics [10]. This software will be briefly introduced and discussed in section 3.1.

[2] Measure to define the size of a spot, where FW_{50} is the diameter of the spot that contains 50% of the beamlet current [7]. Other percentages and methods could be applied, but usually taking a number like 50% is much better than 100%, since only an irrelevantly low number of particles could be scattered extremely far from the center of the spot.

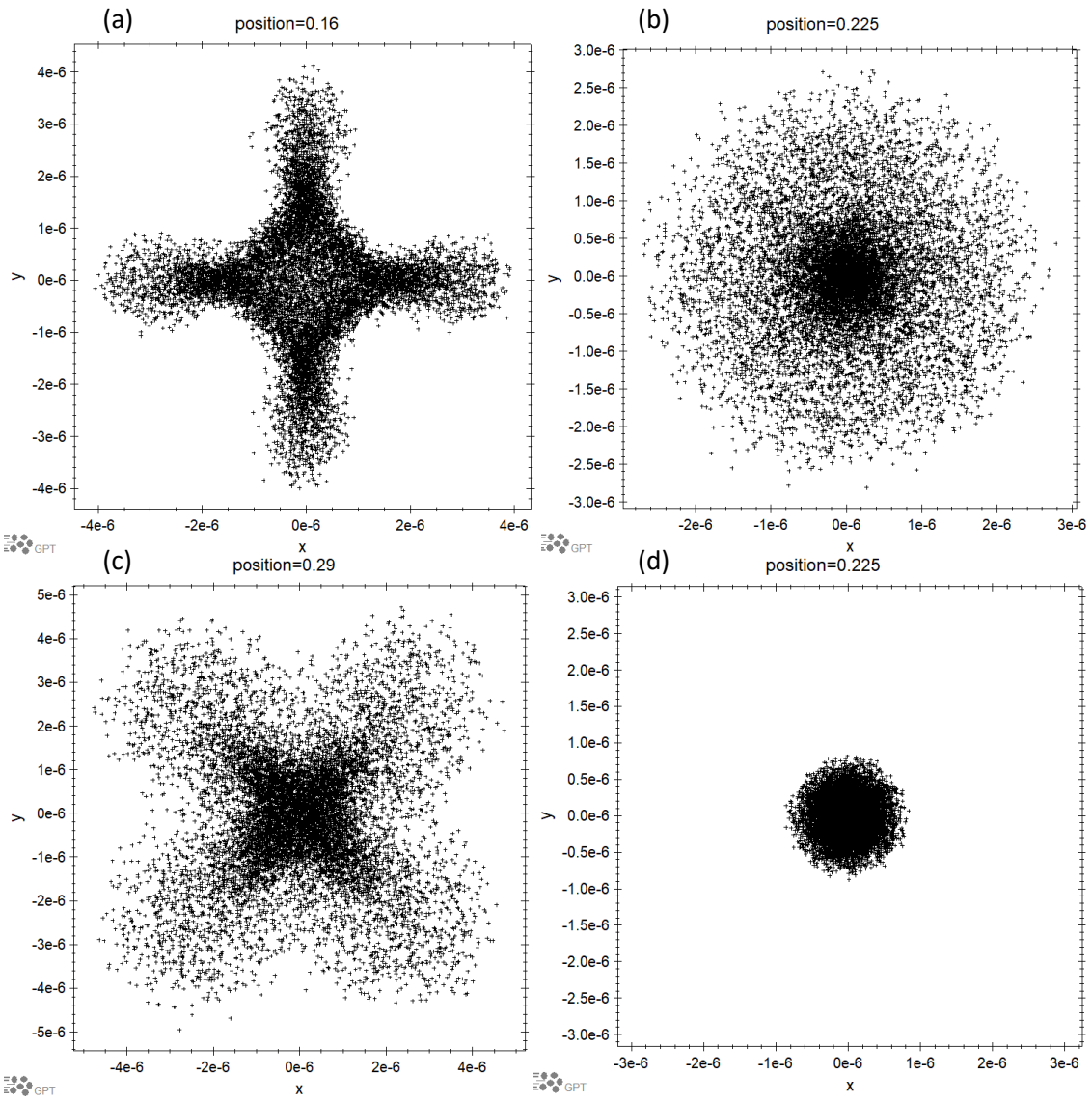

Figure 4: Simulation results of the octupole aberration caused by an ALA: In the first plane positioned before focus (a), the weaker focal strength in horizontal and vertical directions results in an image which resembles a + sign, and the x sign which follows after focus (c) results from particles in diagonal directions that have already passed the optical axis to form the outer ends of this shape. The top right figure (b) depicting the focal point shows the round spot in focus, where the size is enlarged due to particles being scattered in both directions. Figure (d) depicts the spot that is focused by a single aperture lens, without neighbor apertures.

Figure 5 a, b and c show the experimental verification of the octupole effect in focused, over- and under-focused spots at the MBS image plane. To produce these experimental images, the MBS (the same MBS as the one simulated to produce Figure 4) has been mounted in a stand-alone vacuum setup as shown in Figure 6. To see the individual spots, a YAG screen is mounted in the MBS image plane. An (optical) objective lens, looking at the YAG screen, creates magnified images of the individual multi beam spots onto CCD camera.

In section 2.2, a simple method is first used to compare the octupole field strength between an analytical approximation and a simulation and it was found that the analytical approximation is inadequate to

substitute for more time consuming simulations in section 2.3. In section 2.4, a simpler geometry is briefly discussed as a potential alternative to isolate the octupole effect instead of simulating the entire MBS. In section 2.5 the multipole field expansion itself is addressed as a method to eliminate the octupole aberration. The fitting procedure used here has its limitations and is thus not preferred over the more widely applicable plane-to-plane optical path fitting procedure that is discussed in section 2.6. However, the field fitting method will be used for discussion in section 5.3.

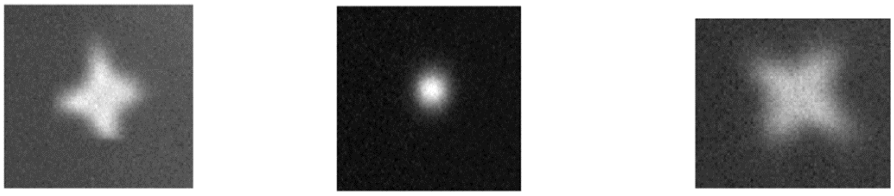

Figure 5: octupole aberration in an experimental MBS setup. The images depict the same spot in different planes after the MBS. The asymmetric charge distribution around closely packed aperture holes leads to an octupole aberration that is observed as a star shaped spot before (left) and after focus (right). In focus (middle), the round spot is enlarged by the octupole aberration and after focus the aberration is inverted. This figure was obtained in an expiremental setup by Ali Gheidary and colleagues at the Delft University of Technology, but has not been published so far.

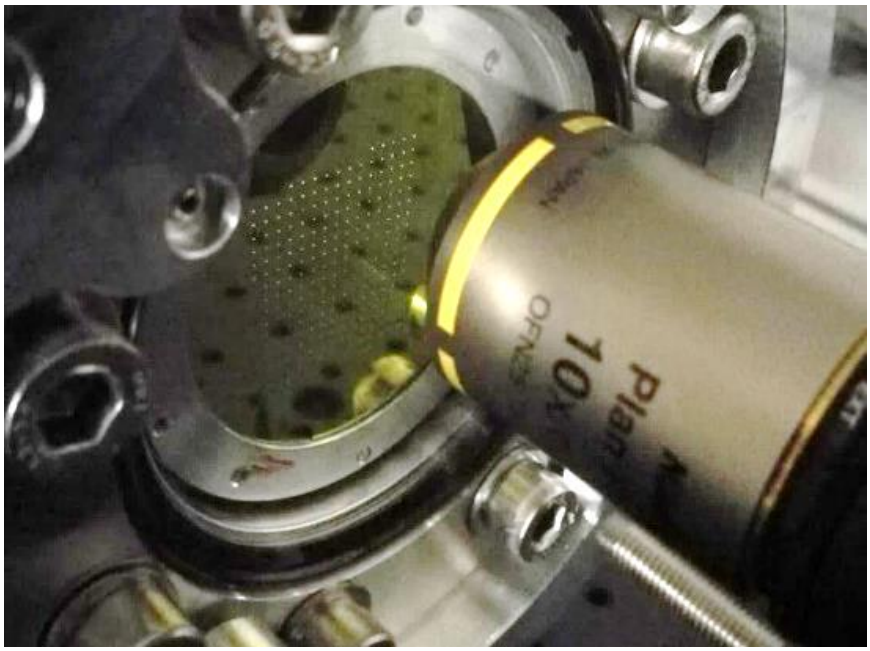

Figure 6: A setup to see MBS spots. The picture is taken from [9] with permission. A YAG screen is used to capture the image of the beamlets projected by the multibeam source onto its image plane (instead of being accelerated by the accelerator lens, being the next step of the SEM as depicted by Figure 2).

2.1 The octupole aberration

The resolution of an electron optical system is limited by defects causing unwanted deflections of particles that cause the particles to be spread over a larger area than what would otherwise be expected when trying to image the initial particle source plane to the sample plane. The octupole aberration that is a major defect in an ALA is first introduced here from a basic optical system. A simple optical system is depicted in Figure 7. Here, two trajectories for particles emitted from a point source located at $z = z_0$ are drawn. Before reaching the first optical element at $z = z_1$, the particles will have an x-coordinate that

linearly scales with the initial transversal velocity $\dot{x}_1$. For an ideal lens, the amount of deflection to the particles between $z = z_1$ and $z = z_2$ then scales linearly with the x-coordinate of particles at the middle of the lens $\frac{z_1+z_2}{2}$. This implies that trajectories originating from a point at z_0 (given that this is a coordinate further from the lens than the focal distance) are imaged to a single point at z_3. However, there can be aberrations in the lens that cause more (or less) deflection than desired. This is illustrated by the blue curve.

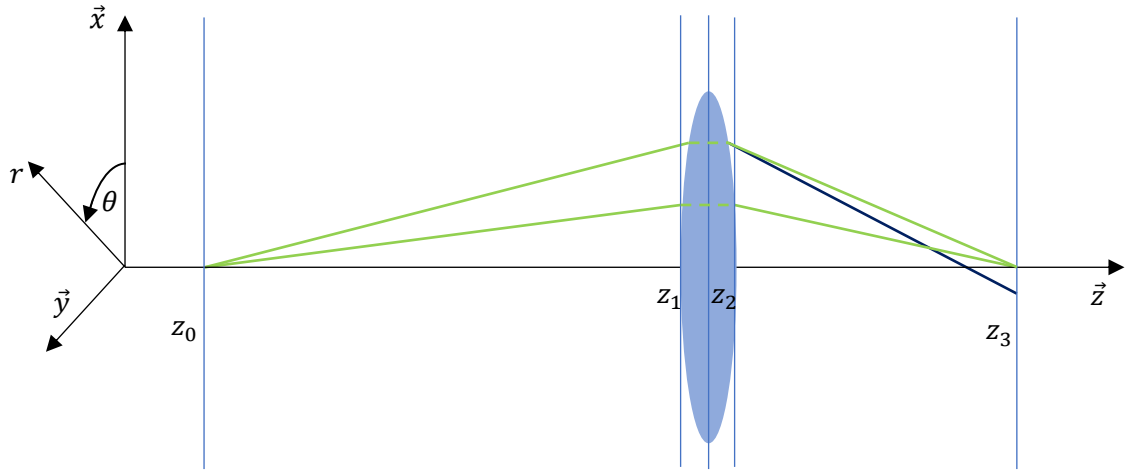

Figure 7: Single lens imaging of electron. The optical system is drawn in the standard cartesian system, and the directions of the cylindrical coordinate representation are shown here as well.

To describe aberrations near an electromagnetic lens, the electric field that causes deflections are examined. The electric potential can be separated into different multipole terms [11], where the monopole ($\phi_0(z)$), quadrupole ($\phi_2(z)$) and octupole ($\phi_4(z)$) terms are given by

$$\begin{aligned}\Phi = \phi_0 - \frac{1}{4}(x^2+y^2)\phi_0{}^{(2)} + \frac{1}{64}(x^2+y^2)^2\phi_0{}^{(4)} - O\left(\phi_0{}^{(6)}\right) \\ + \frac{1}{2}(x^2-y^2)\phi_2 - \frac{1}{24}(x^4-y^4)\phi_2^{(2)} + O\left(\phi_2^{(4)}\right) \\ + \frac{1}{24}\phi_4(x^4-6x^2y^2+y^4) - \frac{1}{480}\phi_4^{(2)}(x^2+y^2)(x^4-6x^2y^2+y^4) + O\left(\phi_4^{(4)}\right).\end{aligned} \quad (2)$$

The higher indices $\phi^{(n)}$ indicate the n -th derivative with respect to the z-direction and the lower index $\phi_m^{(n)}$ indicates the degree of rotational symmetry. For example, by transforming to cylindrical coordinates using $r^2 = x^2 + y^2$ and $\tan\theta = \frac{x}{y}$ (Figure 7), the octupole term $(x^4 - 6x^2y^2 + y^4)$ can be rewritten as $r^4\cos(4\theta)$, which explains the lower index ϕ_4. Because the design for an ALA is typically 4-fold symmetric in θ around the central aperture, the expected multipole contributions for this aperture are also expected to be symmetric multiples of 4-fold symmetry (8-pole, 16-pole, 24-pole, etc.). The quadrupole term ϕ_2 causes a linear deflection for x and y, but it induces a different focal strength for the x and y directions, called astigmatism, which can focus the beam horizontally in a different z-plane than vertically, thereby effectively enlarging the spot. Though this is not a contributing factor for the central aperture, the off-axial beams can have astigmatism through a combination of a lower degree of geometric symmetry around an off-axial aperture, the beam not traveling straight through the aperture and other factors.

Now the deflection for an octupole aberrated lens are derived. For non-relativistic particles[3], the change in the x-velocity, given by $\dot{x}_2 - \dot{x}_1$ between positions z_2 and z_1 respectively, through lens action is

$$\dot{x}_2 - \dot{x}_1 = \frac{q}{m}\int_{z_1}^{z_2} E_x\, dt = \frac{q}{mv}\int_{z_1}^{z_2} E_x\, dz, \tag{3}$$

where the integral of the x component of the electric field E_x can be rewritten as an integral over z, assuming constant particle velocity $v_1 \approx v(z) \approx v_2$ and $\dot{x} \ll \dot{z} \approx v$ (paraxial approximation). Using $\vec{E} = -\nabla\Phi$ and substituting only the lowest order monopole and octupole terms, while changing time derivative $\dot{x}$ to z-derivative x' (again paraxial approximation) gives

$$x_2' - x_1' = \frac{q}{mv^2}\int_{z_1}^{z_2} \frac{1}{2}\phi_0^{(2)}(z)x(z) - \frac{1}{24}\phi_4(z)(4x(z)^3 - 12x(z)y(z)^2)\, dz. \tag{4}$$

Assuming a thin lens[4], the particle positions $x(z)$ and $y(z)$ are held constant within the lens (thus dependence (z) is replaced with a lower index (x_1 and y_1) for the z-position at the lens plane, and can be taking out of the integral, resulting in

$$x_2' - x_1' = P_0 x_1 + P_4(x_1^3 - 3x_1 y_1^2),$$
$$\text{with} \tag{5}$$
$$P_0 = \frac{q}{2mv^2}\int_{z_1}^{z_2}\frac{1}{2}\phi_0^{(2)}dz = \frac{q}{2mv^2}\left[\phi_0^{(1)}\right]_{z_1}^{z_2} \text{ and } P_4 = \int_{z_1}^{z_2}\frac{4}{24}\phi_4 dz$$

where P_0 and P_4 indicate the integrated monopole and octupole terms respectively. Here, P_0 shows the fundamental property of an ideal (aperture) lens where the deflection scales linearly with x, and the strength is determined by the difference in electric field strength before and after the aperture ($\left[\phi_0^{(1)}\right]_{z_1}^{z_2}$), which is the reason why an aperture with a different electric field on either side works as a lens in the first place. After $P_0 x_1$ in eq. (5), an arbitrary amount of (multipole) aberrations can be incorporated. Here, this is only an octupole aberration.

Now similarly,

$$\dot{y}_2 - \dot{y}_1 = \frac{q}{m}\int_{z_1}^{z_2} E_y\, dt \tag{6}$$

leads to

$$y_2' - y_1' = P_0 y_1 + P_4(y_1^3 - 3y_1 x_1^2). \tag{7}$$

Then, the radial deflection $r_2' - r_1'$ is given by the inner with unit vector $\hat{r}$ as

$$r_2' - r_1' = \hat{r}\cdot\begin{pmatrix} x_2' - x_1' \\ y_2' - y_1' \end{pmatrix} = P_0 r_1 + P_4 r_1^3\cos(4\theta), \tag{8}$$

[3] Though in an electron microscope the electron velocities can reach relativistic velocities, this is not the case inside the MBS where typical electrode voltages are smaller than 10 kV.

[4] For an electron optical system in the paraxial approximation, typically the z-velocity, $\dot{z}$, is much larger than the tangential x-velocity, $\dot{x}$ .In a thin lens, particles entering the lens will have roughly the same x, y coordinates throughout the lens, and this displacement can thus be neglected.

with $r_1 = \sqrt{x_1^2 + y_1^2}$. For particles traveling along the x or y axes, $\cos(4\theta) = 1$, the octupole contribution will exactly be the opposite of the diagonal directions, where $\cos(4\theta) = -1$. Because of the field free region after the lens, r_2' is constant and thus, the radial position after the lens is given by

$$(z) = r_1 + \left(z - \frac{z_1 + z_2}{2}\right) r_2'. \qquad (9)$$

The radial positions for particles traveling exactly along the $\cos(4\theta) = +1$ and $\cos(4\theta) = -1$ planes after the lens are denoted r_+ and r_- and are given by

$$\begin{aligned} r_+ &= r_1 + \left(z - \frac{z_1 + z_2}{2}\right)(r_1' + P_0 r_1 + P_4 r_1^3) \\ r_- &= r_1 + \left(z - \frac{z_1 + z_2}{2}\right)(r_1' + P_0 r_1 - P_4 r_1^3). \end{aligned} \qquad (10)$$

This difference in radial deflection for particles along the r_+ and r_- directions results in a 4-fold symmetric star shape spot, as depicted in Figure 8. By measuring the positions of particles in the minimum and maximum deflected positions of this spot, and filling them in as r_- and r_+ in equation (10) it is possible to deduce the octupole strength from a relatively simple measurement. However, when eliminating the octupole, the goal is to minimize the octupole strength, in which case it is no longer possible to leave out other terms from equation (2) than just the first lensing term and the first octupole term. Moreover, the aim of octupole reduction is generally to optimize the spots in the focal plane, whereas the star-shaped contours are only observed at out of focus planes. This calls for a more elaborate fitting procedure, where more aberration terms can be extracted.

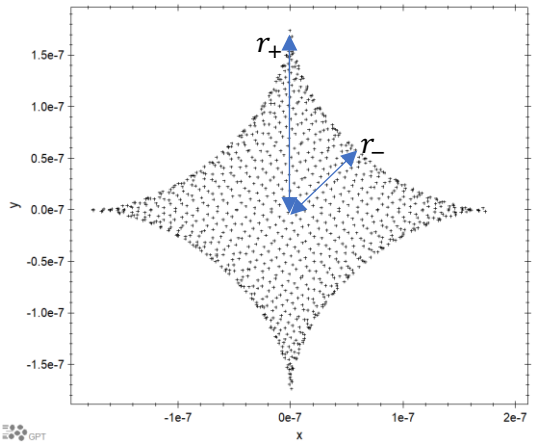

Figure 8: typical star-shaped spot before focus. Radial distances r_+ and r_- are drawn to give a measure for the octupole aberration.

2.2 Analytical approximation for multiple holes in a plate compared to a simulation equivalent

With full 3D simulation software (e.g. BEM+GPT from Pulsar Physics), it is possible to simulate the Octupole effect very accurately. However, due to the complexity of the MBS geometry, the computation time can be very long depending on the required accuracy. Because of this, it is worth the effort to see if an analytical approximation can achieve similar results. A setup consisting of two charged conducting

plates, where one of the plates contains an aperture lens array with 3x3 apertures is used to explore how well the MBS can be approximated analytically. This geometry is depicted in Figure 9, where the two plates are drawn in blue on the left-hand side. The surface charge distribution is displayed on the right-hand side. The charge around an aperture in a conducting plate, which is responsible for the fields in equation (2) is highest (on an absolute scale) near the edges of an aperture. The blue regions around the edges of the aperture are thus expected to exert the highest electric force on the passing electrons. Even though the fields nearby this geometry carry a significant octupole aberration in the region where electrons pass the lens field, the charge distribution around apertures appears to be rotationally symmetric: the blue region around an aperture is (roughly) equally thin in all directions, and also the density (color) is roughly the same all around the edge. If indeed the charge density closely around an aperture in the conducting material is indeed rotationally symmetric around the aperture, the (blue) ring of charges is hardly affected by the presence of nearby holes. Hence, it seems justified to compare the fields that are calculated using a simulation for the 3x3 aperture array to an approximation, which can be made by constructing an array of holes that do not influence each other. For a single aperture (in an infinitely thin, infinitely large conducting plate) there is an analytical expression that can be used for this comparison. In this section, an analytical approximation for the fields near an ALA is constructed and in section 2.3 this is compared to a simulation result.

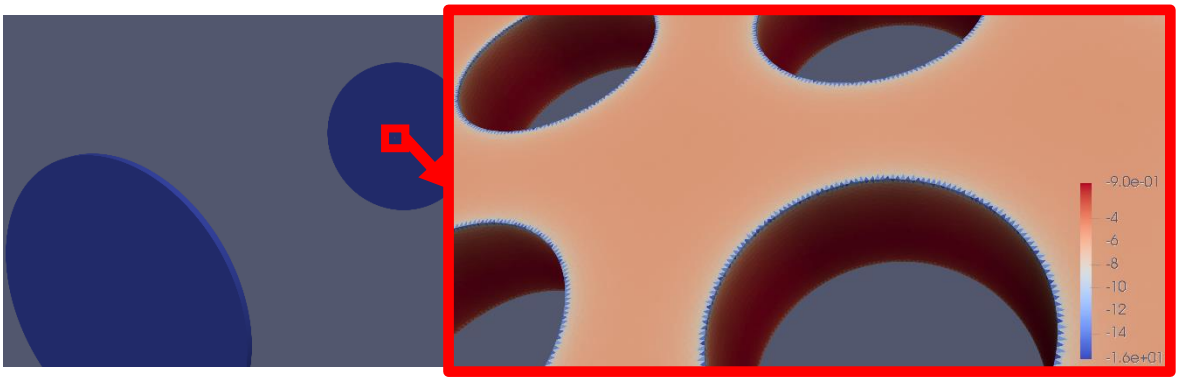

Figure 9: 2-plate geometry simplification. The fields are generated by applying 2 different voltages to the two round plates displayed in this figure. The enlarged section (enclosed by the red rectangle) displays the ALA itself, and the charge distribution for the 3x3 array of holes. The charges built up near the hole seem to be relatively localized near the hole edges, which serves as a motivation for a comparison between a BEM result and a sum of single hole electric potential functions. The charge densities are unitless normalized values, that are used to compute the fields when the geometry is used in GPT. On a relative scale they do represent the charge distribution, and thus e.g. indicate that most of the charge is localized around the edges of an aperture.

For an infinitely thin, conducting infinitely large flat plate with a single round hole, exposed to constant electric fields from on sides, as depicted in Figure 10, the electric potential is given by [12]

$$\phi = \begin{cases} -E_0 z + \delta\ (z > 0) \\ -E_1 z + \delta\ (z < 0) \end{cases}, \qquad (11)$$

where E_0 and E_1 represent the constant electric field strength to which the field converges away from the hole, for z coordinates higher and lower than 0 respectively. Given any radial distance r from the z-axis and hole diameter a, this geometry has an analytical solution which is derived in [12] as

$$\delta(r,z) = \frac{(E_1 - E_0)a}{\pi}\left[\sqrt{\frac{R-\lambda}{2}} - \frac{|z|}{a}\tan^{-1}\left(\sqrt{\frac{2}{R+\lambda}}\right)\right], \qquad (12)$$

where

$$\lambda = \frac{1}{a^2}(z^2 + r^2 - a^2) \text{ and } R = \sqrt{\lambda^2 + \frac{4z^2}{a^2}}$$

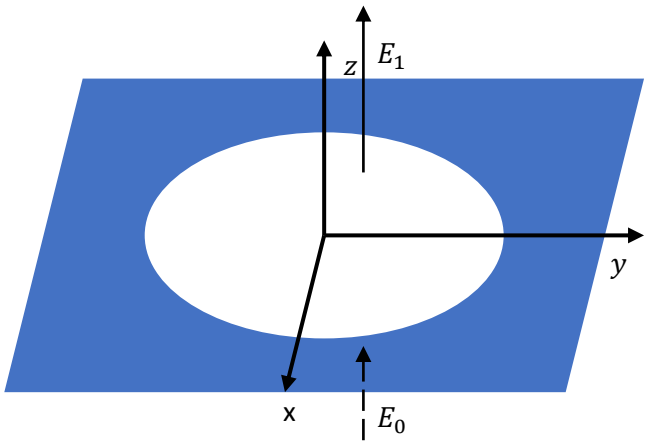

Figure 10: Infinitely thin and infinitely large flat plate with a hole

The charge density effects of an aperture are strongest near the edges of an aperture. For this reason, it may be possible to approximate an aperture array by a sum of displaced versions of $\delta(r, z)$, which is done by substituting $r = (x - nD)^2 + (y - mD)^2$, where D is the pitch between apertures. This substitution allows the approximation of the potential by the influence of the aperture array as

$$\Phi = \begin{cases} E_0 z + \sum_{n,m=-1}^{1} \delta\left(\sqrt{(x-nD)^2 + (y-mD)^2}, z\right) & (z > 0) \\ E_1 z + \sum_{n,m=-1}^{1} \delta\left(\sqrt{(x-nD)^2 + (y-mD)^2}, z\right) & (z < 0) \end{cases}, \qquad (13)$$

where δ remains described by (12). Here, n and m take integer values from -1 to 1 to represent the 9 contributions from a 3x3 aperture array.

The comparison between this crude approximation and the simulation is done by building a simple geometry with a 3x3 micro-apertures ALA in the BEM+GPT electrostatic field simulation package. For this purpose, a 2-plate geometry is built, which is displayed in Figure 9. Because the two plates have a much higher radius than the size of the ALA, the fields along the plate should be roughly constant for distances of the order of the aperture size. This means that near the apertures themselves, the fields should resemble those near an infinitely thin, infinite plate with holes. In this geometry, the radius of a single hole is 10 µm, the pitch between holes is 30 µm and the plate thickness is 10 µm. The resulting charge distribution nearby the hole is also displayed in Figure 9. The comparison is done in section 2.3.

2.3 Multipole effect by nearby apertures: analytical and numerical comparison

Because the radius of the plates, as depicted in Figure 9, is relatively small compared to the distance between them, the field strength is not simply given by $E_0 = \frac{\Delta\Phi}{d}$. In order to find both electric field strengths E_0 and E_1, the simulation result itself is used to find the electric field strengths on both sides of the ALA. For the given simulation, the voltage difference $\Delta\Phi$ is 4000 V and the separation between then

plates is 11mm. Then the field strengths before and after the aperture plate are found by reading the electric potential for several positions in a ring near the aperture, for several z-positions. These rings of positions are represented by Figure 11.

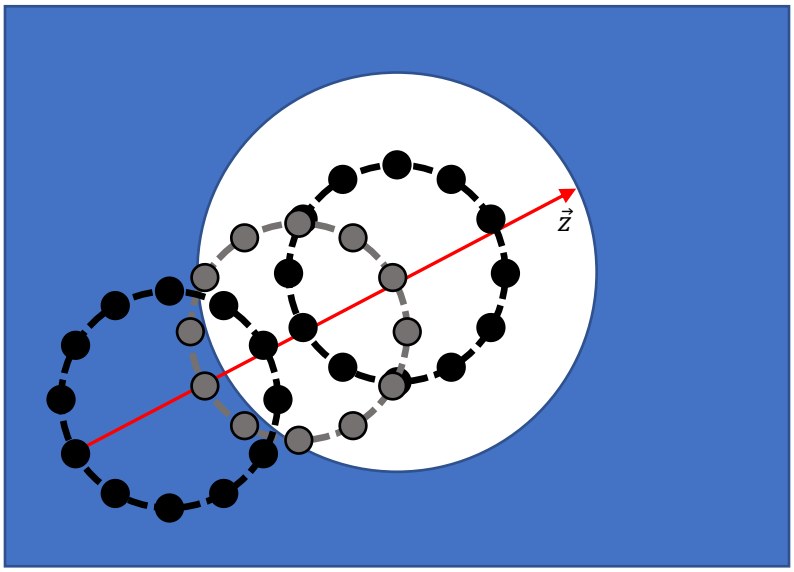

Figure 11: Rings of points near the aperture, for multiple values of z. These can be used to calculate e.g. the average potential for a given z, but also octupole information. The 12 dots drawn in this picture represent the 100 different points on the ring that are actually used, for 100 z-planes instead of just 3.

From Figure 12 it is clear that the slope of the electric potential becomes constant, while the differences in electric potential around the ring drop at only a few times the aperture radius away from the aperture. Thus, the field strength there can be used to fit values for E_0 and E_1 in equation (13). These field strengths before and after the plate are found to be 9.4×10^5 V/m (indeed higher than $\frac{\Delta\Phi}{d} = 3.6 \times 10^5$ V/m) and -9.0×10^5 V/m respectively and when plugged in E_0 and E_1 in equation (13), this leads to an analytical approximation for the fields near the ALA. The same procedure of reading the potential at points on a ring for different z-positions near the central aperture is applied to the analytical approximation. The averaged electric potential from this procedure is also depicted in Figure 12. At $z = 0$, the curve for the field around an infinitely thin plate (orange) bends in a single interval[5], whereas the fields obtained through the more cumbersome BEM procedure in GPT is bent around in 2 short intervals, with a field free region in between.

[5] Though the bend is relatively sharp compared to the simulation result, it is not mathematically sharp (no discontinuity in the derivative). The electric potential inside the aperture is continuous, but the infinitely thin conducting plate does have a discontinuity in the electric fields (before and after) through the material of the infinitely thin plate.

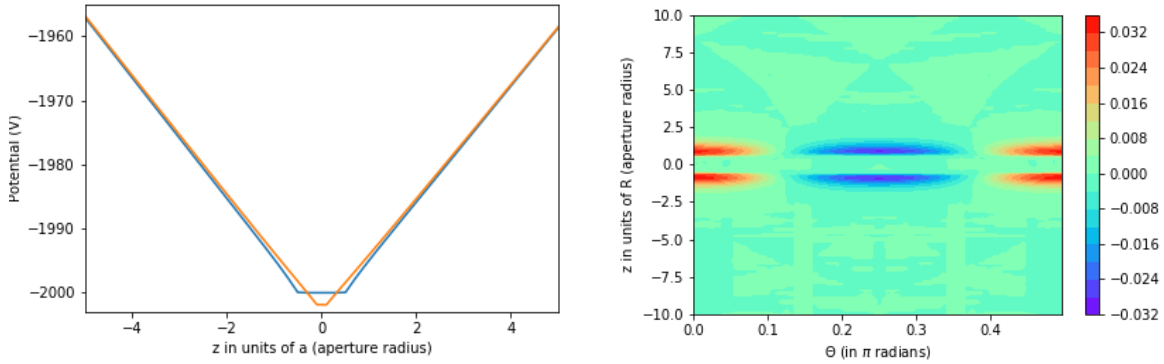

Figure 12: Left: averaged potential for a ring of particles around the z-axis. The orange curve displays the behavior for the field around an infinitely thin plate, while the blue curve shows the behavior around a plate with a finite thickness. The blue curve bends twice to accommodate the change in electric field strength, while the other bends in a more localized region. Right: The electric potential in V on one quarter of a full ring around the optical axis for the simulated geometry. The average values (displayed left) have been subtracted for each ring to allow the more subtle differences for different θ to show. The same "flat" region around z=0 (taken at the center of the aperture) is observed here, and the octupole aberration drops a few times the aperture radius away from the hole.

By calculation of the potential on a ring it is now also possible to compare the octupole strength. This is also illustrated in Figure 13: the left figure depicts the average potential on a ring of points, and the right figure depicts the voltage on all points for all points on all rings minus the average potential for points on that ring. The average value for a given z coordinate is thus always 0 in this figure, allowing the relatively small octupole to become visible, which drops quickly drops to 0 for z-coordinates away for z-coordinates far away from the aperture. The octupole can be quantified by a linear projection of the cosine function $f = \cos 4\theta$ on the electric potential along the ring of points distributed by θ for all z-coordinates. This is a rather crude method for several reasons: there is no distinction between the first and higher order octupole strength, and because of that, choosing an appropriate radius for these points is rather tricky. Therefore, this method was later abandoned.

However, this experiment does lead to an interesting comparison. The octupole resulting from this method is plotted along z, for the analytical approximation and the more cumbersome boundary element method in Figure 15. As can be seen in the figure, the field free region inside the aperture as portrayed in Figure 14 is visible here as well. The difference in octupole strength is found by dividing the integral over the z-coordinate of both functions, and results in a factor of 1.7.

This difference could be due to a number of things, such as the finite thickness of the aperture plate which could, by introducing a field free region, allow a higher surface charge density to become located on the edges of the apertures and effectively lowering the charge density in the flat regions away from the apertures. Then because of the relatively higher concentration of charges near neighbor apertures instead of the flat material around an aperture, this could lead to a higher octupole aberration. Moreover, though the ring of higher surface charge density (blue) along the edges of an aperture appears to be rotationally symmetric, there might be slight variations in density around the aperture, which are not clearly observable in a surface charge plot, that effectively increase or decrease the octupole strength. The reason may be difficult to pin-point, since the surface charge distribution around conducting shapes can be hard to predict simply by intuition or an analytical approach, which is the reason simulations are used here in the first place.

This result serves as a motivation to stop pursuing the approximation of the final solution through addition of analytically derived functions, and instead switch to numerical simulation completely. If the result for both methods would have been close, a likely approach would have been to approximate additional shapes such as walls around holes (discussed in section 4.3.2) as a homogenous ring charge. This is unfortunately not simply possible.

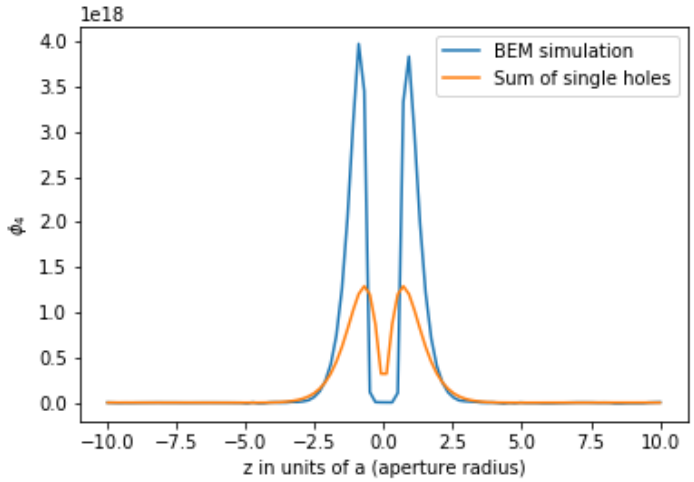

Figure 15: Octupole field strength in $\frac{V}{m^4}$ near a simulated array of holes (blue), versus an approximation through a sum of 9 holes in an infinitely thin plate.

2.4 Simple test case

In the electron source used for this research, the electrons are seem to originate from a small virtual point, known as virtual source with a typical FW_{50} size of 50 nm, whereas the apertures in the ALA have a diameter of 15 µm. This means that most of the spread of the electrons is caused by the angles of the electrons initially, and the finite size of the source can be considered to add undesired "blur" in the final spot. In order to mimic the whole electron source to a simpler case, one might thus want to create a geometry where an infinitely small source (or a source small compared to the other dimensions in the geometry) is placed inside a simplified version of the source. This example using two plates is depicted in Figure 9. A few complications exist with such a simplification, which are explained in this section.

In this simplified geometry the electrons are generated in front of the first plate and the ALA holes are "drilled" into the second plate. Then, assuming the electric field between the two plates E_0 is roughly constant and given by

$$E_0 = -\frac{(\Phi_2 - \Phi_1)}{d} = -\frac{\Delta\Phi}{d}, \qquad (14)$$

where Φ_1 and Φ_2 represent the potentials for the first and second plate respectively and d represents the distance between them. For particles emitted at $r = 0$ and $z = 0$, the initial radial velocity ($\dot{r}_0$) is assumed constant and small compared to the z-velocity ($\dot{z}_0$), while the z-acceleration between the plates is given by

$$\ddot{z} = -\frac{q\Delta\Phi}{md}, \qquad (15)$$

where m is the mass and q represents the (negative) charge of the electron, which solves to

$$z = -\frac{q\Delta\Phi}{2md}t^2 + \dot{z}_0 t. \quad (16)$$

Solving t for particles approaching the second plate at $z = d$ gives

$$t = \frac{\dot{z}_0 \pm \sqrt{\dot{z}_0^2 - \frac{2q\Delta\Phi}{m}}}{\frac{q\Delta\Phi}{2md}}, \quad (17)$$

where the parabolic shape of the $z(t)$ implies a second crossing, which does not occur due to discontinuation of the constant field strength after the second plate. This means only the minus-signed solution will occur, with a radial position near the aperture of $r_1 = \dot{r}_0 t$. The z-velocity ($\dot{z}_1$) at the front of the aperture plate (beginning of the lens) is found by substituting (17) into the first time-derivative of (16) and is given by

$$\dot{z}_1 = \sqrt{\dot{z}_0^2 - \frac{2q\Delta\Phi}{m}}. \quad (18)$$

This amounts for the drift region of this geometry. Then, using (8) for the approximation of an ideal lens (no octupole, only using P_0), the deflection in the lens is given by

$$\dot{r}_1 - \dot{r}_0 = \frac{q}{2m\dot{z}_1}(E_1 - E_0)r_1, \quad (19)$$

where now the electric field strengths before and after the lens are written as E_0 and E_1 respectively and $\dot{z}_1$ is not squared because this is $\dot{r}_1 - \dot{r}_0$ instead of $r_1' - r_0'$. If the radius of the two plates is large compared to the distance between the plates d, then the (constant) electric field strength between the plates can be approximated by $E_0 \approx -\frac{\Delta\Phi}{d}$. In Figure 12, the slope in potential is roughly equal and opposite in sign, thus giving $E_1 = -E_0 \approx -\frac{\Delta\Phi}{d}$.

Then substituting $\dot{z}_1$ and r_1 in (19) gives

$$\dot{r}_1 - \dot{r}_0 = -\frac{q\Delta\Phi}{md}\dot{r}_0\left(\frac{\dot{z}_0 - \sqrt{\dot{z}_0^2 - \frac{2q\Delta\Phi}{m}}}{\frac{q\Delta\Phi}{2md}}\right)\left(\frac{1}{\sqrt{\dot{z}_0^2 - \frac{2q\Delta\Phi}{m}}}\right), \quad (20)$$

which can be reduced and rearranged to

$$\frac{\dot{r}_1}{\dot{r}_0} = \left(\frac{2\dot{z}_0}{\sqrt{\dot{z}_0^2 - \frac{2q\Delta\Phi}{m}}} - 1\right). \quad (21)$$

For the particles from a point to be able to be focused back to a point, the radial velocities before and after the lens have to be related inversely by $\frac{\dot{r}_1}{\dot{r}_0} < 0$, thus requiring

$$\frac{2\dot{z}_0}{\sqrt{\dot{z}_0^2 - \frac{2q\Delta\Phi}{m}}} < 1, \quad (22)$$

which does not have any real solutions. The square root here implies that for a ΔV high enough to focus the particles after the second plate, there will be a potential difference over the plates too high for the particles to reach the second plate at all. Instead of assuming $E_1 = -E_0$, It might be possible to alter the geometry or voltages such as to change value α in $E_1 = \alpha E_0$ to lower values than -1 in order to satisfy (22) and create a spot. However, this could require more complicated geometries, and in the end results in a situation where most of the focusing effect is dependent on the field *after* the aperture lens, whereas in the real situation this region is to be assumed field free, while all of the octupole aberration (correction) is introduced in the region *before* crossing the aperture plate. Because of these complications involved in making a simplified geometry to learn about the octupole effect, this approach is abandoned, and a more realistic version of the MBS is simulated immediately.

2.5 Potential function multipole expansion fitting

For the octupole aberration of the electric potential near an ALA, a comparison between an analytically derived approximation, and a more accurate Boundary Element Method (BEM) incorporated in GPT is drawn in Section 2.3. Though this method suffices to demonstrate the difference in strength of the fourfold-symmetric field effect, there is no assertion for correctness of these multipole coefficients in an absolute sense. For example, when using a ring of particles with a fixed radius about the z-axis to fit the octupole strength, the numerical value for the first octupole ϕ_4 (2) will be linearly dependent with the second octupole term $\phi_4^{(2)}$. In order to get rid of this issue, one might read the potential at a sufficiently large number of positions, and arrange them as

$$\begin{pmatrix} \Phi_1 \\ \Phi_2 \\ \vdots \\ \Phi_m \end{pmatrix} = \begin{pmatrix} 1 & -\frac{1}{4}(x_1^2+y_1^2) & \dots & \frac{1}{24}(x_1^4-6x_1^2y_1^2+y_1^4) & \dots & F_{n,1} \\ 1 & -\frac{1}{4}(x_2^2+y_2^2) & \dots & \frac{1}{24}(x_2^4-6x_2^2y_2^2+y_2^4) & \dots & F_{n,2} \\ \vdots & \vdots & & \vdots & \ddots & \vdots \\ 1 & -\frac{1}{4}(x_m^2+y_m^2) & \dots & \frac{1}{24}(x_n^4-6x_n^2y_n^2+y_n^4) & \dots & F_{n,m} \end{pmatrix} \begin{pmatrix} \phi_0 \\ \phi_0^{(2)} \\ \vdots \\ \phi_4 \\ \vdots \\ f_n \end{pmatrix}, \qquad (23)$$

where $F_{n,m}$ indicates the n-th fitting function incorporated to approximate the electric potentials Φ_m at all m locations and f_n is the value for any aberration term incorporated, including the octupole ϕ_4. Abbreviating the first vector with Potential values as P, the matrix with polynomials M and the vector with aberration values as A, this equation can be solved as a least squares fitting method by [13]

$$A = (M^T M)^{-1} M^T P, \qquad (24)$$

given that enough different positions are included to make the equations linearly independent. ($m \geq n$).

Though this approach can be used to fit multipole values to the electric potential, the effect on the beam is not fully explored in this method. For thin lenses, it is possible to integrate $\phi_4 = \int \phi_4(z)dz$ and optimize the geometry such that the octupole $P_4 = 0$. However, the octupole will only be gone if the thin lens approximation made to get equation (5) holds. However, in practice, there might be significant off-axial particle motion, thereby invalidating the thin lens approximation. In that case, requiring $\phi_4 = \int \phi_4(z)dz$ =0 is not accurate enough to eliminate octupole aberration. Moreover, this method runs into problems when applied to off-axis holes. For off-axis holes, the optical axis is not always perpendicular to the ALA, and thus correction of a multipole in the electrostatic potential when integrated along an axis taken

constantly perpendicular to the ALA does not carry the information relevant to fit all multipole values. Moreover, getting rid of aberrations such as "regular" two-fold astigmatism by correcting for the quadrupole term in the potential fitting result, in general doesn't mean that there is no astigmatism in the final spot. As touched upon in section 2.1, this can be due to the off-axial trajectory of the beam in a combination with higher order monopole expansion terms around the z-axis.

Alternatively, aberrations can be corrected by tracing particles and fitting aberrations to the particle positions themselves, similarly to the method described by equation (23). This method is addressed in section 2.6.

2.6 Plane to plane beam aberration fitting

The wave-front of a wave-like particle electron beam at the image plane ψ_{im} is related to the object plane ψ_{obj} through

$$\psi_{im} \propto \psi_{obj} \exp(-2\pi i\chi), \tag{25}$$

where χ is the phase aberration function representing the extra phase shift of the wavefront due to the lens aberrations. This can be converted to the wave aberration by $W = \frac{\lambda\chi}{2\pi}$, which through conversion with wavelength λ represents the optical path difference of waves [14].

The wave aberration can be expanded to a linear contribution of its nonlinear aberration components. This is typically done by a collection of terms where $w_0 = x_0 + iy_0$ represents the complex initial particle position and $\omega_0 = \omega_{x0} + i\omega_{y0} = \frac{p_{x0}+ip_{y0}}{q_0}$ the initial transversal particle momentum. These coordinates allow polynomial expansion in the following form [15]

$$\begin{aligned} W = \Re\Big\{ & A_0\bar{\omega} + \frac{1}{2}A_1\bar{\omega}^2 + \frac{1}{2}C_1\bar{\omega}\omega + \frac{1}{3}A_2\bar{\omega}^3 + \frac{1}{3}B_2\bar{\omega}^2\omega + \frac{1}{4}A_3\bar{\omega}^4 + \frac{1}{4}B_3\bar{\omega}^3\omega \\ & + \frac{1}{4}C_3\bar{\omega}^2\omega^2 + \frac{1}{3}B_{31}\bar{\omega}^2\omega w + \left[A_{0c}\bar{\omega} + \frac{1}{2}C_{1c}\bar{\omega}\omega + A_{11c}\bar{\omega}w\right]\frac{\Delta\Phi}{\Phi} + \cdots\Big\}. \end{aligned} \tag{26}$$

Here, C_1 represents defocus, C_3 represents spherical aberration, and higher C_i terms represent higher order cylindrically symmetric aberrations. Likewise, first order astigmatism terms are grouped by A_i, where A_3 represents octupole aberration and terms indexed c indicate first order chromatic aberrations; $\frac{\Delta\Phi}{\Phi}$ is the relative variation of accelerating voltage. The image aberration Δw_{im} or particle (extra) deflection can then be computed through differentiation of this term [15] [5]:

$$\Delta \mathrm{w}_{\mathrm{im}} = -M\left(\frac{\partial W}{\partial \omega_x} + i\frac{\partial W}{\partial \omega_y}\right) = -M\frac{2\partial W}{\partial \bar{\omega}}, \tag{27}$$

where M is the magnification. Though very similar in notation, the aberration terms fitted by the particle tracing program GPT discard the wavelike background and behavior of these equations, and instead directly map particle positions from plane to plane through a fitting procedure that minimizes

$$\mathrm{S}^2 = \sum_i \left\| w_i - \sum_{\substack{j\le k,l,m,c \\ j+k+l+m+c \\ <order}} w_{jklmc,i} \right\|, \tag{28}$$

where particle i is traced to xy-position w_i, and $w_{jklm,i}$ are the contributions from different aberrations. The x-y coordinate w_i is equal to $\Delta \mathrm{w}_{\mathrm{im}}$ evaluated for the initial conditions of particle i. The expanded

aberrations $w_{jklm,i}$ are defined through a potential like aberration function that resembles (2) where the terms are given by

$$\psi_{jklmc}(x', y', x, y, \delta) = \left(\frac{\Delta\Phi}{\Phi}\right)^{c} (x'^2 + y'^2)^{\frac{j+k}{2}} (x^2 + y^2)^{\frac{l+m}{2}} (C_{jklmc} \cos\varphi - D_{jklmc} \sin\varphi) \quad (29)$$

with

$$\varphi = (j-k) \arctan\left(\frac{y'}{x'}\right) + (l-m) arctan\left(\frac{y}{x}\right).$$

The x and y components of $w_{jklmc,i}$ are then given by $\frac{\partial \psi_{jklmc}}{\partial x'}$ and $\frac{\partial \psi_{jklmc}}{\partial y'}$. Because of the linear independence of aberration terms $w_{jklmc,i}$, the aberration coefficients C_{jklmc}, D_{jklmc} can be found with the same procedure as presented in (23) and (24), where vector P is now filled with all positions w_i and matrix M with the polynomials $w_{jklmc,i}$. Though there is a notational difference between equations (26) and (29), both cover the same solution space and there is high similarity between the two. In equation (29), the octupole contribution is represented by $\psi_{4\,0\,0\,0\,0}$, while it is A_3 in equation (26). For this reason, $C_{4\,0\,0\,0\,0}$ is called A3r and $D_{4\,0\,0\,0\,0}$ is referred to as A3i in GPT. Because the apertures are arranged in an x-y aligned grid, A3i does not appear (or any other D_{jklmc} terms in our geometry, because these terms, contrary to the design, are all asymmetric in the x-plane). Similarly, the quadrupole term $\psi_{2\,0\,0\,0\,0}$, or "regular" astigmatism is represented by A1r and A1i for the $C_{2\,0\,0\,0\,0}$ and $D_{2\,0\,0\,0\,0}$ respectively.

3 Numerical procedure

The simulation procedure contains several numerical accuracy settings in order to achieve reliable aberration results, that allow the elimination of the octupole aberration. An overview of GPT and the newly developed BEM tools is given in section 3.1. Using this program, an optimization of two numerical settings has been done, which are the chamfering value and the BEMsolve tolerance. These parameters play an important role in making sure the electric fields calculated for the MBS are sufficiently accurate for fitting the optical aberrations and will be described in sections 3.2 and 3.3. The results of those optimizations are presented in section 3.4. The octupole aberration is largest when the aperture has a filling factor of 100% (when the VA is removed). However, a small radial margin of the aperture near the edges of the aperture is still not used by the simulations, which is discussed in section 3.5. Finally, an experimental image from a spot produced using a corrected ALA is compared visually to a simulated equivalent in section 3.6.

3.1 GPT and BEMdraw

GPT is a well-established simulation tool for the design of accelerators and beam lines. GPT is based on 3D particle tracking techniques, providing a solid basis for the study of all 3D and non-linear effects of charged particle dynamics in electromagnetic fields [10]. The program allows the incorporation of relatively simple shapes such as analytical models of infinitely thin plates with an aperture as depicted in Figure 10, or analytical descriptions of electrostatic or magnetic multipoles to study the beamlines of for example particle accelerators and in our case, electron optics. Recently, a combination of tools has been added that allows the construction and optimization of electrostatic conducting free forms in GPT. These different tools are briefly addressed in this section.

In order to construct 3D shapes, in the first place a programmable drawing tool is required. Though a collection of 3D drawing programs were readily available, most programs did not fit the requirements for this application. One prevalent problem is that some drawing programs do not very well support the construction of shapes with high accuracy on different length scales in the same shape. For example, the MBS electron source is typically multiple millimeters long. For the regions of the source where the beam is not close to the material (the outer corners of the partially displayed cylinder as depicted in Figure 21), the features of the material do not always have to be drawn accurately down to sub-micrometer accuracy. In the ALA however, a sub-micrometer defect can completely determine the result, as is evident from the sensitivity to the correction shapes that will be discussed in section 4. Contrary to the BEMdraw tool developed by Pulsar, most 3D drawing programs will simply allow the specification of the accuracy by a single feature size parameter, that will draw too much computational effort to relatively unimportant areas. BEMdraw instead, allows the specification of the maximum angle between two adjacent triangles on a curved surface, which is more suitable for this application. For this reason, it is very helpful to have a program that allows forcefully adding more detail at some places, as is described in section 3.2. In addition to this drawing procedure, the next step is transforming the drawn shape into one suitable for simulation purposes. This process is depicted in Figure 16, where the construction of a single ring-shaped electrode is depicted. The left half (blue) is the output from BEMdraw, which is a set of triangles that make up the surfaces of a 3-dimensional ring. The triangles are the output of the drawing procedure and the surface described by the triangles describes the outer surface of the electrode to within a design accuracy. This means the boundaries of the ring shape are accurately defined. However, the mesh is not yet optimal for simulation. For example, a single triangle connects the inner radius to the outer radius of the ring, which does not allow the calculation of charge densities along this direction of the surface. Furthermore,

the sharp shape of the same triangle is numerically unfavorable. For these reasons, the same surface must be redistributed into smaller triangles, which is called remeshing. The right half (white) of Figure 16 depicts the result of this step. In remeshing procedure, the program adds triangles by splitting up larger sharply pointed triangles, to add enough triangles to simulate the charge distribution of a continuous charge distribution along a conducting ring, while making triangles as equilateral as possible.

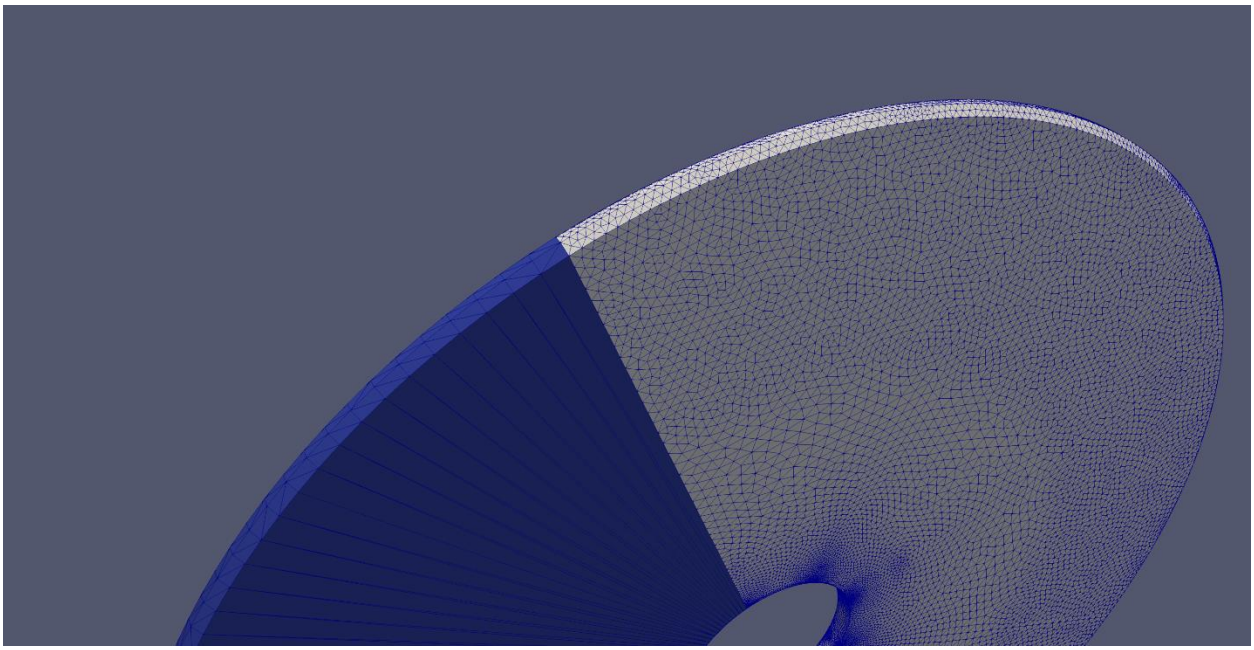

Figure 16: Remeshing of a ring shaped electrode. The left (blue) side is the geometry as provided by BEMdraw. The remeshing result is displayed in the right side of the image.

The next step in our simulation is calculating the charges along the surfaces of these 3D shapes. Because of the field free inner regions of our conducting shapes, a boundary element method (BEM) is more favorable over a finite element method, which would require a 3D distribution of tetrahedron-like shapes filling up the entirety of the shapes. Instead, the triangles making up the surface of each conducting shape carry all the charges of the shape, which allows a BEM approach. The way this works and an important accuracy parameter are described in more detail in section 3.3.

Finally, the charge distribution calculated for each shape is used to trace particles. The fitting procedure that uses the collection of terms in equation (29) to fit all aberrations from the source plane to the image plane, was still under development by GPT during the start of my graduation project. This is the reason different approaches such as calculating the octupole fields using the electric potential on a ring of points (section 2.3) were initially tried in the first place. The next step was reading the electric potentials in an array of z-planes and doing the fitting procedure as described in section 2.5. When Thermo Fisher Scientific received the fitting tool that does the aberration fitting procedure as described in section 2.6, the script incorporated all terms described by equation (29) up to certain polynomial order to calculate the optical aberrations. Typically, there are hundreds of terms present that do not contribute, such as a hexapole in a 4-fold symmetric geometry, which are eliminated by the fitting tool in a time-consuming procedure. Some of my modifications and suggestions such an option to exclude all D_{jklmc} terms were incorporated in the newest version of this GPT fitting procedure, along with an electric field fitting option as described in section 2.5.

The output of the fitting procedure is a list of aberrations along with a value C_{jklm} and D_{jklm}, along with a "blur" value for each aberration. This blur is calculated using the deflections $\frac{\partial \psi_{jklmc}}{\partial x'}$ and $\frac{\partial \psi_{jklmc}}{\partial y'}$, which are a function of initial coordinates $(x_i', y_i', x_i, y_i, \delta_i)$ for a particle i, by

$$blur_{jklmc} = \sqrt{\frac{\sum_i^N \left(\frac{\partial \psi_{jklmc}}{\partial x'}(x_i', y_i', x_i, y_i, \delta_i)\right)^2 + \left(\frac{\partial \psi_{jklmc}}{\partial y'}(x_i', y_i', x_i, y_i, \delta_i)\right)^2}{\mathrm{N}}}, \quad (30)$$

where N is the number of particles. This value is thus the root mean square deflection of the particles in the spot, due to an aberration indicated by indices $jklmc$. Because of the different polynomial orders of different aberrations, the order of magnitude of an aberration itself does not tell a lot about the magnitude of contribution by an aberration. The blur allows users to compare the deflections on a meaningful length scale and determine which is the most relevant.

3.2 Edge chamfering value

The drawing and BEMsolver tools supplied by Pulsar physics contain a remeshing tool that transforms the three-dimensional design into a mesh suitable for simulation. Because of the asymptotic behavior of charge and field effects near sharp edges on a surface, the sharp edges are computationally more expensive to solve, and require more attention for accurate results. This can be seen in Figure 9, which depicts an aperture array with walls (discussed in section 4.3.2). The charge density on flatter surfaces around the apertures and on the cylindrical inner surfaces of the aperture is relatively constant. However, the charge density sharply increases 5 orders in magnitude at the blue convex rims of the walls around the apertures, compared to the red concave edges that connect the flat plate to the walls around the apertures. This distribution is typical for conducting surfaces: due to the self-repelling nature of positive and negative surface charges, a higher amount of charge can accumulate on a convex surface or rim because that is where less repelling force from other parts of the material will be felt. This makes the charges around a sharp edge numerically difficult (or in some case impossible) to compute accurately. Simply increasing the number of triangles near a sharp edge may thus not be the best way to calculate the charges in order to accurately represent the charges around a 90° angle. In order to calculate the charge distribution around sharp angles accurately, all edges near the electron beam are numerally chamfered. This method is depicted in Figure 17. The chamfered edge forces a smaller feature size near the sharp edges of the aperture, which causes the remeshing tool to include more triangles near the edge. At the same time, the blunted angle causes a slightly less steeply evolving charge density across the edge. When the size of the chamfered corner is small enough, this does not effectively change the shape of the geometry, while making the problem computationally faster and more reliable.

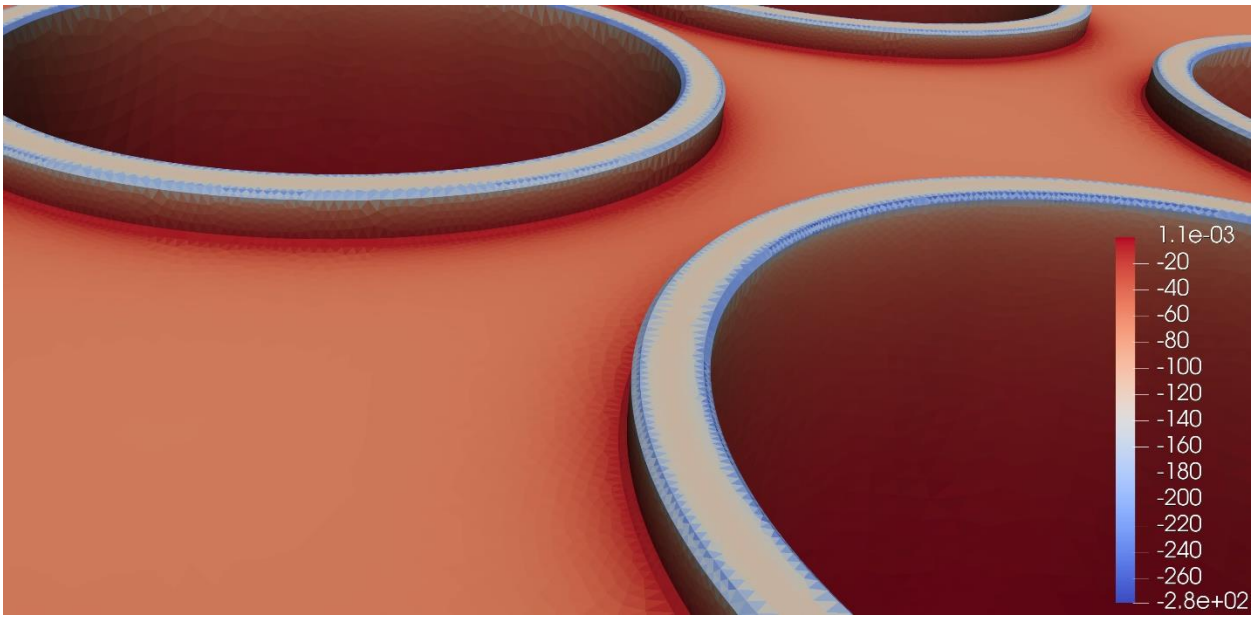

Figure 17: chamfering of edges in a geometry with aperture walls. The solution for the charge density (unitless normalized quantities) induced by the nearest electrode set at 1V has been used as a color scale in this figure. Due to the chamfered edge, the charge density changes more gradually across the edges of the aperture compared to an edge without chamfering.

3.3 BEMsolve tolerance

The Boundary Element Method solver (BEMsolve) used in this work [16] calculates the surface charge density σ_i at each triangle i. Because the voltages applied to the different electrodes could change between different simulations, the charge distributions and electric fields will change as well. This means that when the electric fields are calculated for a single configuration of voltages, this time-consuming process has to be repeated when different voltages are used. Instead BEMsolve takes a different approach. The main algorithm of the BEM solver calculates the equivalent uniform surface charge density of each of the triangles such that the potential is 1 V on one electrode and 0 V on all other electrodes. In our case where there are 6 electrodes, this results in an output file where a collection of 6 charge density distributions is stored for the whole geometry. The resulting charge density can subsequently be fed into GPT to describe the complete 3D fields. In GPT, an input file is used to set the actual settings for the potentials. The final resulting charge distributions are thus calculated by scaling the charges for unit potentials with the actual voltages applied to the electrodes and adding all 6 contributions from the 6 voltages applied to the 6 electrodes.

Because the charge densities are stored in a 6-fold solution where there is always only one electrode at 1 V and the others at 0 V, this is also what the charge density plots such as in Figure 29 depict. In our case, this is not important: the configuration is such that the nearest electrode at 1V completely carries all information about the charge density on the ALA. This is because the ALA itself is always at 0 V, and the second nearest electrode induces surface charges that are one or more orders of magnitude lower on the ALA. Therefore, in order to qualitatively compare the charge distribution on the ALA, this is good enough.

The charge distribution is solved numerically using

$$V_j = \sum_i M_{ij}\sigma_i, \qquad (31)$$

where V_j should, after correct calculation of charge density values σ_i, be equal to the unit potentials U_j that are known beforehand for each triangle j, and where matrix element M_{ij} describes the electrostatic repulsion/attraction force due to charges on triangles i and j. Though the vector containing all elements σ_i, fully describes the surface charges around a surface, it is a normalized (unitless) quantity to avoid multiplying and dividing by the vacuum constant, electron charge and pi (present in the description of M_{ij}) which would slow down computation and could increase the risk of rounding errors. Instead, GPT uses the unitless charge densities σ_i (which is also depicted in all 3D figures that show a charge distribution) to compute the fields when particle tracing starts. σ_i is found by inversion of M_{ij}. Because the program aims to work with large amounts of triangles, the matrix M_{ij} is never stored in full in memory. Instead, an iterative solver is used such that only the result of the matrix multiplication $M\sigma$ is needed. This inversion thus leads to a result for all charge densities σ_i, where there is a discrepancy between $\sum_i M_{ij}\sigma_i = V_j$ and U_j.

The iterative solving process stops when the residual precision given by

$$\sqrt{\frac{1}{N}\sum\nolimits_j \left(\left(\sum_i M_{ij}\sigma_i\right) - U_j\right)^2} < \epsilon \qquad (32)$$

has reached the target setting value of ϵ. Here, N is the number of triangles. This means that this precision value is an important accuracy parameter. The BEMsolver allows n-th fold symmetry in the geometry to be accounted by solving only 1/n-th of the whole geometry (Because the geometry for a square ALA grid is 8-fold symmetric, the input geometry for the charge solver is also 1/8th of the whole geometry, speeding up the simulation or allowing higher precision (lower ϵ) in the same time. Termination of the iterative charge solver leaves residual errors which, when copied symmetrically into all 7 other directions, results in an octupole aberration. For this reason, an octupole contribution to the electric field as a numerical artifact is to be expected, even for a cylindrically symmetric design. This illustrated in Figure 18, where a single aperture is drawn such that the color of each triangle represents the residual error $\left(\sum_i M_{ij}\sigma_i\right) - U_j$ for that triangle. Indeed, there is a fourfold symmetric residual error around the aperture.

Though this may sound as a disadvantage introduced by simulating only part of the geometry, it is not: simulation of the whole geometry instead of 1/8th does not mean there will not be an octupole erroneously introduced numerically. Instead, using the same ϵ for the whole (1/1-th of a) geometry instead of 1/n-th will result in the same root mean square precision in the voltages V_j across the surface and thus the electric fields which scale linearly with V_j will be wrong by the same proportion. This means using 1/n-th to calculate charges only speeds up the simulation due to the lower number of triangles involved. The octupole aberration that appears in either case (so full simulation or 1/n-th partial simulation) due to the numerical tolerances in a cylindrically symmetric geometry should thus be representative of the accuracy in the value of this aberration, and is thus used to estimate the effect of the errors in V_j on the spot.

Moreover, a 1/n-th cut-out of the geometry makes sure that only multipoles that are a multiple of n can remain after the charge solving procedure. This is because the charge distribution resulting from copying a partial charge distribution in n directions, will be n-fold symmetric, eliminating multipole terms that do not have this property. For this reason, it is certain that no lower order multipoles (excluding the monopole) than n will be present.

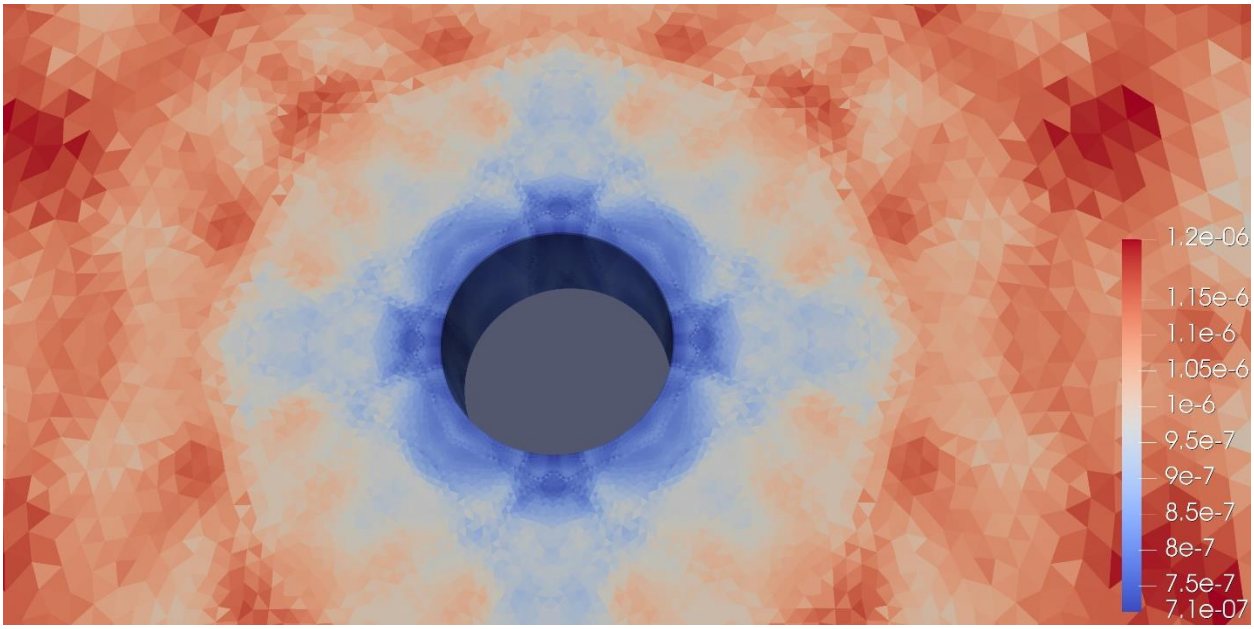

Figure 18: The residual error in V_j in Volt for triangles near a single aperture hole, for the solution where 0 V is applied to the ALA, and 1 V being applied to the nearest electrode. Because the iterative process leaves a residual error in 1/8th of the geometry that is copied to all other directions, the resulting residual error contributes an octupole aberration to the electric field.

3.4 Edge chamfering and BEMsolve tolerance optimization

Though the chamfering of important edges improves the solvability of equation (31), the chamfering itself also changes the geometry, and can induce new field aberrations. For a geometry with a grid of apertures, increasing the chamfer value also increases the octupole effect, since this effectively enlarges the size of the apertures. The "normal" geometry consists of an ALA where the thickness of the plate itself is 10 µm, the pitch between the centers of aperture holes is 20 µm and the radius of the holes is 7.5 µm. By creating 3 different geometries with different chamfer values (the value is equal to the thickness of the edge that is chamfered away), the resulting octupole can be compared, judging from the different fitted octupole aberrations in the procedure in the same plane (in this case at z=30 mm). The resulting octupoles and blur are given in Table 1. The octupole blur is calculated by computing the deflection for the outer particles in the beam due to the octupole aberration in the given plane. Though the blur scales linearly with the fitted aberration, the values in Table 1 do not exactly share this property. This may be due to outer particles being removed from the simulation because the outer edges of the beam itself can be slightly altered due to the influence of a chamfered edge.

As can be seen in the table, a chamfering of 1 µm significantly increases the multipole effect, while this apparently non-linear effect quickly diminishes for lower chamfer values. Between 0.2 and 0.1 µm for chamfering value, the difference is 14 m. This means the error in octupole for a chamfered edge of 0.1 µm will probably be 14 m (or 4% of the octupole) at most, but probably lower. Here, the goal is to eliminate an aberration that, in the case of Figure 4, causes the spot to be enlarged 2.7 times, or 1.7 times for the geometry discussed in section 4. For an optimization where 4% of the 0.7 increasing factor is left, this will leave the spot enlarged by a factor of approximately 1.03 (=1+0.7x0.04, where the factor 0.7 is considered the octupole contribution), which can be considered low enough since other aberrations may become more important at this point. This is thus decided to be accurate enough.

Then by comparing different BEMsolve tolerances for a geometry with a single hole, a tolerance of $\epsilon =$ 2e-6 is found to be sufficiently accurate. For a single hole (so no neighbor apertures) with this tolerance, the residual field defects caused by the iterative charge solver leave an octupole aberration of A3r=-2 m. This is considerably lower than the aberration caused by the chamfering of the edges themselves, and thus also good enough. The upper estimate of 14 m as an error due to chamfering is then used as an estimate of the accuracy in the octupole aberration.

Table 1: Octupole aberration due to different chamfer values in the same plane

Chamfer size (μm)	*A3r (m)*	*Octupole blur (nm)*
0.1	372.28	653
0.2	386.731	661
1	505.995	865

3.5 Positional particle-aperture margins

As described in section 2, the higher order aberrations such as the octupole become dominant when the beam diameter is increased and the ALA approaches (or becomes) the beam limiting aperture. In order to simulate the ALA as a beam limiting aperture, particles are removed from the tracing procedure when they "hit" the aperture membrane instead of passing through the hole. However, the fields generated by the material of the ALA is simulated by treating mesh triangles as point triangles, where the accuracy of the fields calculated by the BEMsolve procedure drops when approaching the mesh "nearby". In this case, "nearby" means when the distance between the electron beam and the aperture wall becomes roughly equal to the distance between the point charges that make up the aperture wall. This effect is somewhat mitigated by the "oversample" setting where a parameter N splits every triangle into N^2 points of equal charge, which makes sure that for increasing N, the fields generated by a mesh triangle approach the field of triangle with a uniform charge density, which supposedly is a better approximation of the fields near a surface than the collection of point charges positioned at only the centers triangles that make up the mesh of the surface.

Even though this effect can thus be limited by oversampling and by reducing the size of triangles at important edges, which in this case is done by the chamfering process, there is a limit to how close particles can get to the surfaces before their trajectory loses its significance. For this reason, particles are removed from the simulation at a z-margin slightly before the aperture plate. For an ideal "thin" lens, particles are only deflected by a lens which changes their transverse velocity, while keeping the transverse xy-position constant. Even though the presence of spherical aberration terms proves this cannot be completely accurate, the simulation result is very insensitive to this parameter.

There is also a radial margin for particles to stay away from the aperture edges when passing the removal plane (at a z-plane slightly before the aperture itself). This radial margin is more important, since from (29) can be seen that aberrations scale directly with some power of the radial distance r. For a larger r-margin, the resulting aberration coefficient should remain the same because the coefficients themselves simply do not depend on r. However, when increasing the margin, effectively decreasing the beam diameter, the higher order aberrations are more quickly lost to numerical noise as they scale with a higher order of r. This means that for a lower r-margin, or larger effective beam diameter, higher order terms can start to contribute. For example, a 16-pole effect or 24-pole aberration can begin to contribute for the 4-fold symmetric geometry of our square aperture array. When lowering the radial margin to 0, we

would effectively have to include an infinite amount of aberrations $\psi_{jklmc}(x', y', x, y, \delta)$ in order to match the source to the image plane.

This also means the contribution of higher order terms that can actually occur, such as 16-pole, will reduce the quality of the fit defined by (28) if they are not included in the fitting procedure and can even lead to the fitting procedure failing. For this reason, the r-margin is chosen with care when fitting optical aberrations. When trying to reproduce an image from experimental results without fitting aberrations, there is more liberty in setting this parameter because it can only start to produce wrong results when particles are as close to the aperture walls as the distance between point charges that make up the wall. In order to optimize octupole correction shapes by fitting the aberrations, a radial margin of 1 μm is generally sufficient to optimize geometry for a chamfering parameter (or typical edge triangle size) of 0.1 μm. This does lead to problems in some cases as is addressed in section 4.3.4.
In principle, the order of aberrations included could be increased instead of increasing the r-margin. However, the tools incorporated by GPT assumes one cannot always know beforehand which aberration terms might be affecting the result, and therefore includes all terms up to a certain order in transverse position and momentum, and then procedurally kicks out terms that do not play a role until a limited set of aberrations specified by a minimum amount of "blur" is included. Currently, the highest possible aberration "order" is set to 6, which excludes the 16-pole (that is of polynomial order 7). If the order is increased beyond 6, the amount of potential aberrations quickly grows from hundreds to thousands, which poses new problems for solving the matrix inversion described by (24).

3.6 Comparison with experimental results

To verify whether the MBS can be simulated accurately enough with the given numerical procedure in order to get rid of the octupole aberration, an experimental result simulated and discussed here. The experiment itself concerns an attempt to get rid of multipole defects. After observing the Octupole effect in simulations and its verification in experiment by Mohammadi-Gheidari, et al. [9], a correction method was proposed based on modifying the shape of the micro-apertures, from round holes into square holes with rounded corners (the same correction method is used for optimization with the new software in section 4.3.4). The parameter to be optimized for this geometry is the separation distance between the centers of the circles that make up the outer corners of the round square or semicircular hole, Δr, as shown in Figure 19a. Δr = 400 nm was found as an optimum value for eliminating the four-fold effect. An aperture lens array with this geometry was made and installed in the MBS experiment. However, the measured spot shape was not found to be round yet. Though the four-fold symmetric effect seemed to be suppressed greatly, higher order contributions, especially an eight-fold symmetric (sixteen pole) effect appeared in the spot shape as shown in Figure 20a. The experimental result did not confirm the prediction of the simulation that resulted in a spot without octupole contribution. This discrepancy remained unexplained for a while. However later it was found that they have not been able to calculate the electrostatic field of the MBS to an acceptable accuracy using the simulation program available at that time, i.e. Opera3D. It also turned out that the parameter Δr = 400nm is not the optimal value.

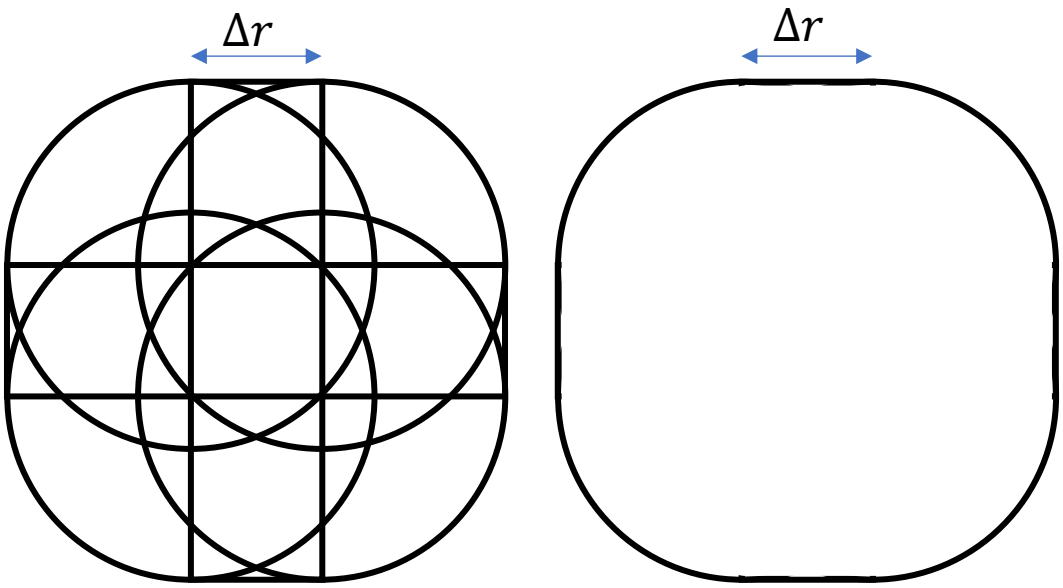

Figure 19: Semicircular hole correction and description of the correction parameter Δr. The distance between the centers of 4 cylinders that form the corners of a rounded square defines the correction relative to the "normal" case of a round aperture. Though the right figure depicts what the aperture ends up looking like, Δr is typically smaller compared to the size of the hole (this is just an exaggeration) and does not make the hole look different from round visually.

The additional tools have been added to GPT, to allow the simulation of the MBS to an acceptable level of accuracy, in order to get rid of the octupole aberration. A MBS similar to the one that is discussed in more detail in section 4 and thereafter optimized to get rid of the octupole, was used to produce the spot visible in Figure 20a. Though the z-position for this image is not precisely known, the design of the MBS and voltages used in the experiment have been used to compare the experiment to the results of a simulation. The result of this simulation is shown in Figure 20b, which depicts the particles scattered for at a z-position where the spot visually matches the shape of the spot seen in an experiment. It appears that, like can be observed in the experimental result, the spot is larger in $\cos(4\theta) = -1$ (diagonal) directions than along the $\cos(4\theta) = 1$ (horizontal and vertical) directions, which is the result of a residual octupole aberration. Moreover, a significant 16-pole aberration appears be present as well, which is evident from the way the spot is pinched in 8 directions. The close visual resemblance and the fact that now the octupole (as well as the 16-pole) appear to be correctly predicted indicate that enough attention has been paid to numerical details at this point to proceed to the optimization of an aperture lens array. This is done in section 5.

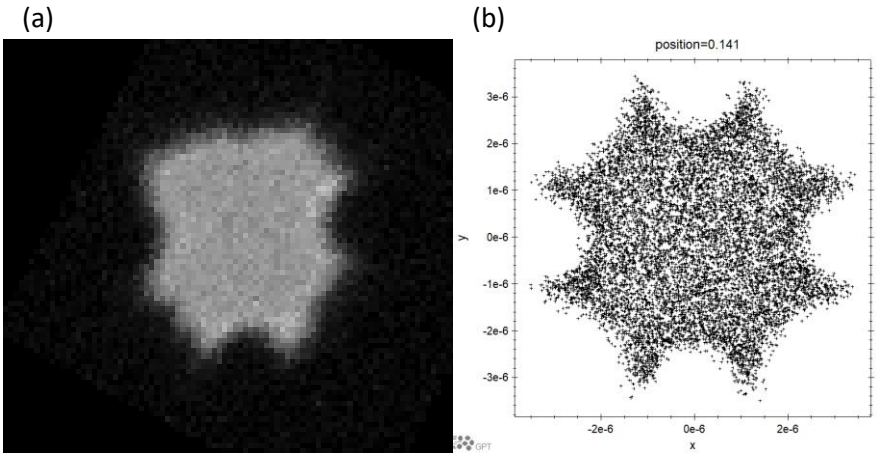

Figure 20: (a): Experimental result of a MBS where a semicircular hole correction shape (depicted in Figure 19) has been applied as an attempt to correct for the octupole aberration. The semicircular hole modification used here is 400 nm.
(b): simulated version of particles traced through the same geometry. The experimental and simulation techniques produce very similar spots.

4 The multibeam source design

In this chapter, the design of the multibeam source is first briefly described in section 4.1. Then in section 4.2 more information about the Schottky electron source in this geometry is given. In section 4.3, the modifications which aim to correct the octupole aberration are described.

4.1 The multibeam source

In Figure 5, the experimentally obtained spot clearly shows the octupole effect, which initially sparked the interest in correcting this aberration. The results of the simulation of this MBS can be seen in Figure 4, which demonstrates that the same effect can be seen numerically. In an effort to correct the octupole, a correction to the ALA design was implemented [9], which resulted in the spot that can be seen in Figure 20, where a remainder of the octupole aberration can be observed.

Recently, a new MBS has been designed, where the geometry and voltages are optimized such that no off-axial aberrations, such as the A1r term, should occur [17]. This optimization has been done for a geometry where, instead of an aperture array, a single aperture is placed at off-axis angles (so not in the center of the geometry) without off-axial aberrations enlarging the spot. For this reason, this design is used to eliminate the octupole in this work, in order to isolate precisely the effect of the aperture array and the corrections being made here.

Unfortunately, no experimental work could be done yet to compare the new design to earlier ones. For this reason, only experimental results are shown of earlier designs. In the remainder of this thesis only results of simulations will be discussed. The goal was initially to optimize and test a MBS in an experiment to verify whether the result of simulations performed here matches experimental observations. However, as mentioned in the introduction, due to limitations posed by COVID-19, this has not been achieved.

In the electron microscope, the MBS is set at a high negative voltage to accelerate the electrons into the optical focusing column. In order to prevent these accelerating fields from penetrating and affecting the

optical properties inside the MBS, another shielding element is constructed around the MBS to create a field free region after the ALA. This means all optical properties of the MBS are determined inside the MBS, and simulations can be isolated to this region. The design of the MBS optimized in this work is shown in Figure 21. The figure depicts 1/8th of the geometry, as this is the portion needed for BEMsolve. The shielding element after the ALA itself present in experiments is not needed here. To create a field free space after the ALA, the voltage of the ALA element (the outer cylinder depicted in Figure 21) is set to 0V. In a functioning microscope, the voltages of all elements in the MBS are lowered by the same accelerating voltage applied to the ALA, which results in the same electric fields inside the MBS.

The electron beam emerging from the Schottky type electron source (depicted by a blue arrow at Figure 21) is first modified by a macro-electrostatic lenses consisting of the extractor, the light blue element (a), two sets of macro electrodes (red and green, or b and c) which both consist of two rings (light and dark). The encasing cylinder (d), colored dark blue, contains the aperture array.

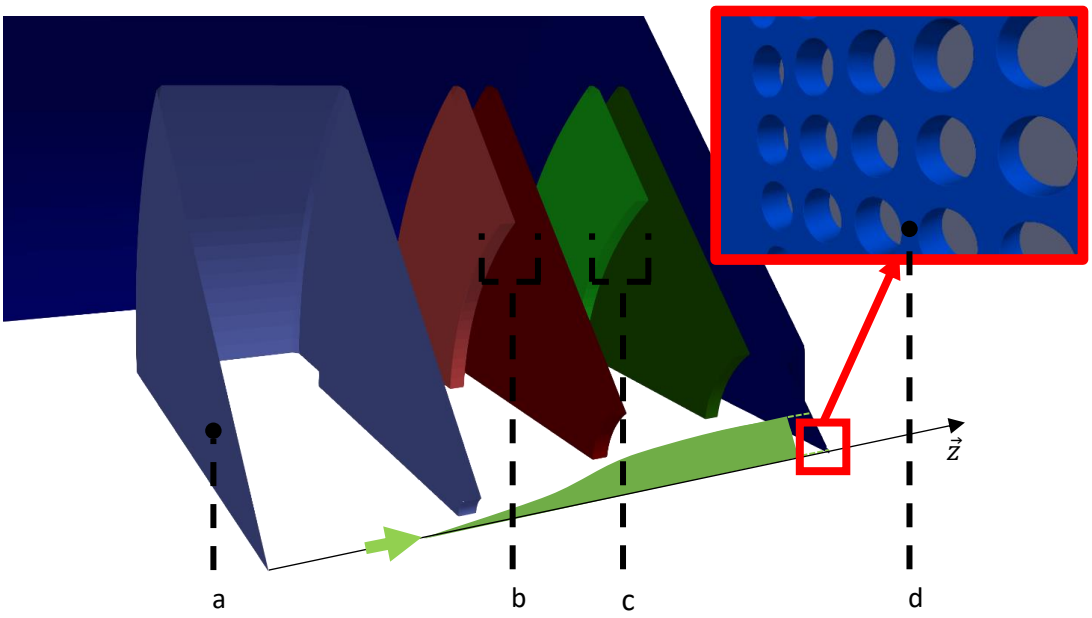

Figure 21: Geometry of the multibeam source. The particles are generated near the light blue element (a) which mimics the real source for a multibeam electron source. The beam is then modified using two electrostatic lenses (red and green, or b and c) which both consist of two rings (light and dark, or left and right). The encasing cylinder depicted in dark blue (d) contains the aperture array, which is consists of µm sized apertures that are not visible when displaying the other (mm sized) elements, hence the enlarged picture of the ALA (indicated with a red arrow) in the top right corner. The light blue shape represents the Schottky source extractor, where the electrons are generated in the virtual source plane, indicated by the green arrow.

4.2 The Schottky electron source

The electrons are generated from a standard Schottky type electron source, which is depicted in schematically in Figure 22 and is adapted from [18]. The Schottky electron source itself is a complicated element in the MBS. The source tip of the source produces electrons through field enhanced thermionic emission at a temperature of typically 1800 K. The source tip, drawn as a pointy end to the source element itself in Figure 22 can have multiple types of shapes, and slowly changes shape during operation. The extractor is placed at several thousands of Volts positive to the source tip to extract the electrons towards the extractor. As the name suggests, the suppressor suppresses emission of electrons at other positions than the source tip in unwanted directions by putting it at a few hundred Volts negative to the tip. The

fields generated between the source tip, the suppressor and the extractor act as a lens. Because of this, the trajectories of the electrons that have passed the extractor appear to come from a different plane (indicated by dotted lines coming together) than the actual source tip from which the electrons are emitted. This plane is called the virtual source and is typically located behind the surface of the source. The source used for optimization to get rid of the octupole effect here is assumed to have a FW_{50} size of 50 nm in its virtual source plane. In all simulations however, the physical electron source and the field are simply replaced with a point source, the virtual source with the same size (FW_{50} = 50 nm). It is located 30 µm behind the physical emitter and the electrons are emerging from this point towards the extractor with an initial energy equal to the potential energy of the extractor. With this simplification, the cumbersome simulation of the emitter is not required.

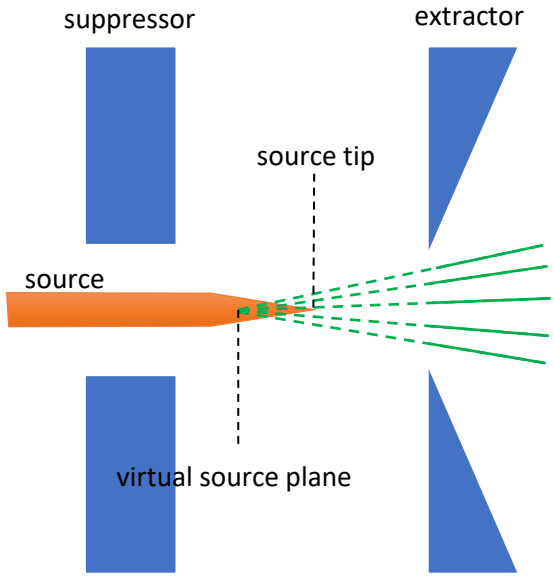

Figure 22: Schematic drawing of a Schottky electron source, adapted from [18]. The source tip produces electrons through field enhanced thermionic emission at a temperature of typically 1800 K. The extractor is placed at several thousands of Volts positive to the source tip to extract the electrons towards the extractor. As the name suggests, the suppressor suppresses emission of electrons at other positions than the source tip in unwanted directions by putting it at a few hundreds of Volts negative to the tip. The virtual source is typically located behind the surface of the source tip itself and is indicated by the crossing dotted green lines.

4.3 ALA multipole correction shapes

In this section, the aperture grid of the ALA is first discussed in 4.3.1. Then, the different shapes that are used to correct the octupole aberration are introduced. The results for these different geometries are discussed in chapter 5.

4.3.1 Reference rectangular array

The ALA depicted in Figure 23 is the only non-cylindrically symmetric element in the MBS and causes the octupole aberration. All apertures in the ALA have a diameter of 15 µm and are distributed orthogonally with a pitch of 20 µm on a (thinned) Si wafer of 10 µm thickness. The array is a set of 25 holes arranged in a 5x5 square pattern. More off-axial apertures could be included here, but this quickly increases computational time required. The 5x5 array is chosen here so the first off axial aperture will have all 8 neighbor apertures and can thus be used to check for residual octupoles and other aberrations.

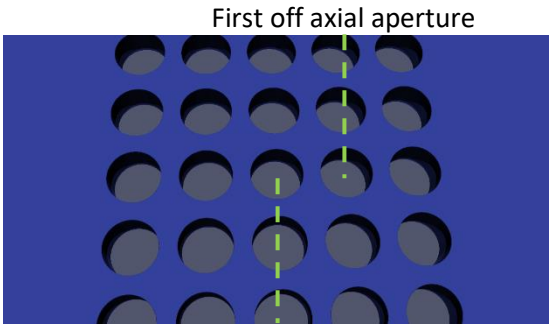

Figure 23: ALA with a regular array of apertures distributed in a square pattern (for simulation we assumed an array of 5x5 aperture holes). The central aperture and first off axial aperture through which particles are traced are indicated.

4.3.2 Aperture Walls

Adding walls around the apertures (see Figure 24) could compensate charge deficits at neighbor aperture locations by adding charges on the rims of these walls, while also potentially providing a barrier around the aperture which shields from field effects by nearby apertures. These walls are parameterized by their height and have a width of 1 µm.

Figure 24: Walls around aperture

4.3.3 Indentations

Assuming the octupole is induced by nearby apertures due to the local relative charge deficit at the position of a hole, the multipole effect could be compensated by adding indentations to cause charge deficits in diagonal ($\cos(4\theta) = -1$) directions. Similarly, to the holes themselves, these indentations are characterized by their diameter. Their depth is held constant at half the wafer thickness. These indentations are depicted in Figure 25.

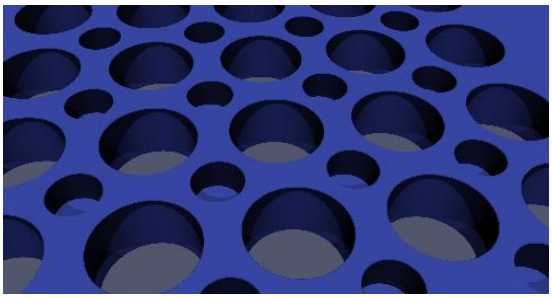

Figure 25: Indentations between holes corners

4.3.4 Semi-circular holes

Though only relatively subtle changes to the aperture shape seem to be required, a counteracting octupole effect can be induced by changing the shapes of the apertures. Instead of cylindrical, the shapes are defined as squares with rounded corners, where the lengths of the squares' sides remain equal to the regular hole diameter. The length of the straight edges of the aperture holes, or distance between the centers of 4 circles forming the corners of the rounded squares are small compared to the diameter of the round holes. The effect is slightly exaggerated in Figure 26 for illustration.

As described in section 3.5, excluding high order fitting terms which do play a significant role in the resulting spot can lead to problems. In the case of semi-circular holes, the radial margin must be increased to fit aberrations, because this shape seems to induce higher order terms such as higher order octupole terms and 16-pole astigmatism near the edges. Though the aberration fitting procedure could in principle be extended to higher order terms (16-pole and others), this will only slow down the fitting procedure, while the goal is to eliminate the octupole, which can be done for a larger r-margin (or smaller effective beam radius).

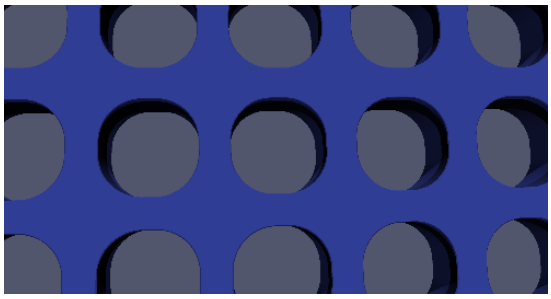

Figure 26: Semi-circular holes

4.3.5 Hexagonal hole pattern

For a hexagonal array of holes, the pitch between neighbor holes is the same as the pitch used for a square aperture pattern. Therefore, the aperture distribution pattern is expected to cause an approximately equal multipole deflection at the edges of an aperture hole. However, because this multipole will be 6-fold symmetric, the strength will also drop with a power six on the radius r for particles closer to the optical axis. The beamlet diameters can be reduced by another aperture array later, thus this geometry might help reduce the effective multipole aberration as well. Moreover, walls have been added around the holes in this geometry to examine the effect of further suppressing the induced 12-pole in this geometry. The thickness of these walls is 1 µm, and their height is variable. The hexagonal ALA pattern, with the addition of aperture walls is depicted in Figure 27.

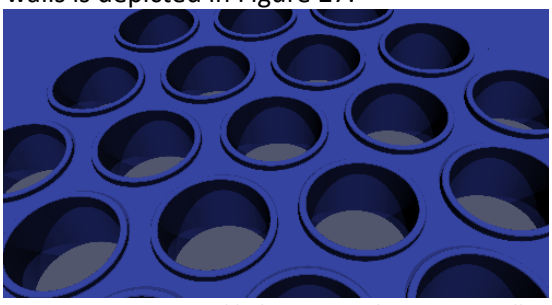

Figure 27: Hexagonal hole array, with aperture walls

5 Optimization of- and comparison between different correction shapes

The optimal correction parameters are calculated and presented in section 5.1. The charge distribution around these optimized apertures is shown and used to calculate the sizes of the spots for the central and first off-axial apertures in section 5.2. The difference between these results is discussed as well.

5.1 Multipole correction parameter optimization

The correction shapes introduced in sections 4.3.2 - 4.3.5 all aim to eliminate the octupole aberration that result in an undesired spot enlargement. Though the reason for the effectiveness of different correction shapes is briefly explained in section 4.3, there is absolutely no guarantee that the methods will work, because the complicated nonlinear behavior of the surface charge distribution that is iteratively solved here, can be difficult to predict. For correction methods that do compensate the octupole aberration as was hypothesized, the behavior of the residual octupole strength as a function of the correction parameters may be highly nonlinear. In this case, optimization can be done by an iterative process where two geometries with a slightly different correction parameter are compared, and the zero-intersection of the octupole strength is determined by interpolation between two points.

The error in the multipole strength is estimated as the same constant value for all points, which is due to the chamfering process (which increases the octupole strength by effectively enlarging apertures). Division of this error by the slope of the aberration between the two points used for interpolation yields the error in the correction parameter. This is consequently equal to the construction tolerance of these different correction shapes, with the accuracy as discussed in section 3.4. The multipole strengths for all correction methods with varying correction parameters are displayed in Figure 28, along with the optimized parameters for all these geometries in the corner of each figure. For the hexagonal hole pattern, this is a 12-pole, similarly to A3r, denoted by A5r. As discussed in section 3.4, the error in A3r is 14 m in all points for the square, which corresponds to a blur (equation (30)) of 24 nm. For the hexagonal hole pattern, this blur can be used to estimate the error in A5r at 6×10^6m.

For aperture walls and semicircular apertures, the data points lie close to a straight line (Figure 28a and Figure 28c). However, this linearity is by no means a known behavior that is to be expected. For aperture walls, the motivation to attempt this correction is the addition of charges around neighbor apertures to compensate the deficits induced by neighbor apertures. Though the surface area of the walls increases proportionally to the height, the charges are mostly located on surface at the top of the walls (as can be seen in Figure 17), which does not increase. Similarly, for semicircular holes, it is rather a surprising incident to see a linear relationship rather than something to be expected.

Because of this, the interpolation between two points is preferred over a linear fit to all data points that might disregard physical effects that contribute nonlinear details. The fact that the relationship seems approximately linear does mean that no further iteration around the zero-intersection is needed with the current precision.

For indentations (Figure 28b) there is a clear curvature in the behavior of A3r. Initial interpolation between indentation widths of 5 µm and 8 µm gives 7.8±0.1 µm as an optimal result[6]. Because of the direction of

[6] Though 7.8 µm lies "just" within the range 7.87±0.08 µm. Still, the tolerance represents an upper limit on the effect of aperture chamfering and thus the new value 7.87 is deemed better.

the curve, the optimal correction value is expected to be slightly higher. For this reason, another iteration is done by interpolation between 7.8 µm and 8 µm is done, where the higher slope yields a lower construction tolerance and the result is 7.87±0.08 µm. For indentations, the relative tolerance is lower than for the other shapes, because of the curvature displayed in Figure 28b. However, on an absolute scale the tolerance for this shape is still the largest, and therefore the least sensitive to construction defects. The nonlinearity in Figure 28b can be explained by the motivation given in section 4.3.3: the area of the indentation quadratically increases with its width, which could result in quadratically increasing charge deficits in diagonal directions.

For the hexagonal pattern, the behavior due to an increasing aperture height appears to deviate from linearity. However, the relative error in the 12-pole is a lot higher than for A3r in a rectangular grid, since A5r induces less blur. The lower blur is to be expected due to the 6-th order dependence on the radial position r for 12-pole field strength. This also leads to a relatively high tolerance in the optimal wall height and because of that, the more nonlinear behavior of this curve for higher wall heights (Figure 28d) can be ignored (no further iteration is required with the given tolerance).

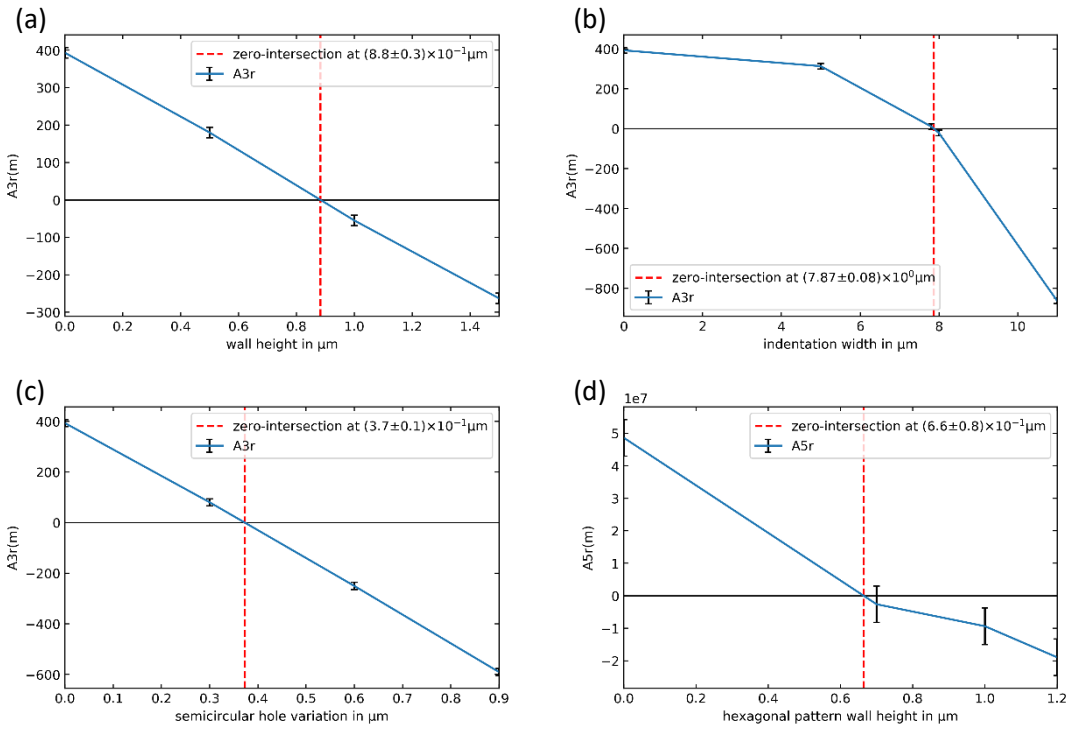

Figure 28: Optimization of the correction shapes. The octupole is depicted for varying aperture wall heights (a), indentations with varying widths (b) and semicircular holes with varying shape values (c) and the 12-pole aberration (A5r) is depicted for varying wall heights around a hexagonal aperture grid (d). The optimal correction parameter is given in the legend of each figure in µm.

5.2 Octupole correction effects on the spot

The optimized parameters that eliminate the multipole aberrations are used to construct optimized geometries. The resulting charge distribution (induced by the nearest electrode set to 1V and the others

to 0V) is displayed in Figure 29 for the regular 5x5 rectangular aperture grid without corrections, and the correction through aperture walls, indentations and semicircular holes.

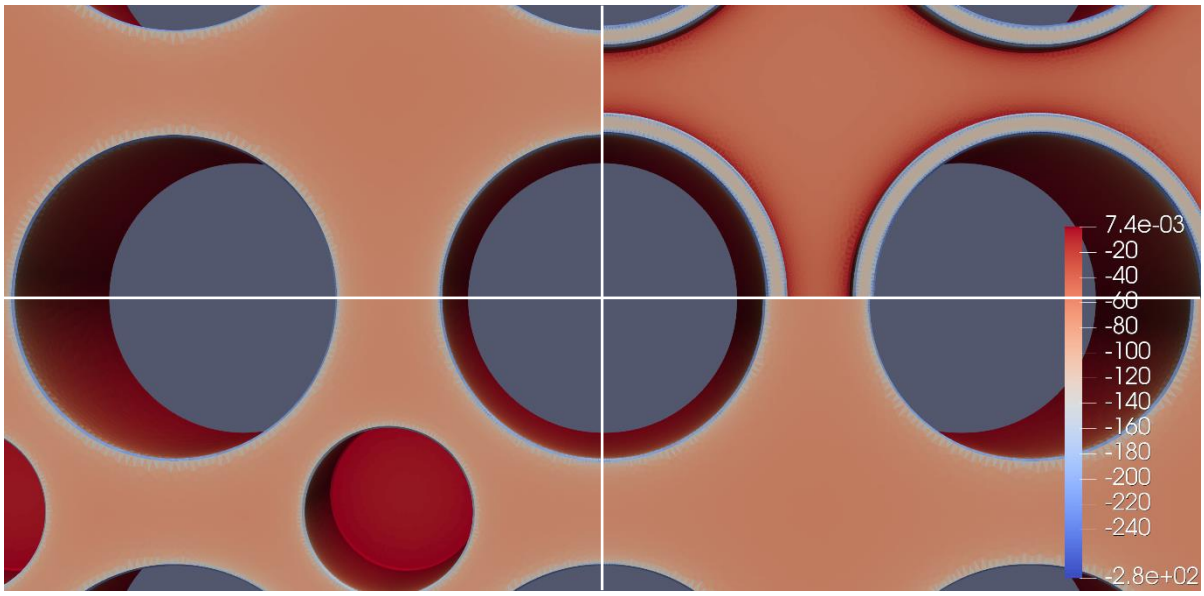

Figure 29: Charge distribution induced by nearest electrode to the ALA. The image consists of four quadrants where the top left presents the reference shape, the top right presents the correction by walls, the bottom left presents the correction by indentations and the bottom right presents the semi-circular holes. The color scale is the same for all quadrants. The highest negative surface charges (blue) are concentrated at the convex rims of the aperture holes.

The highest negative surface charges (blue) are concentrated at the convex rims of the aperture holes. As predicted the walls appear to compensate (negative) charge deficits introduced by nearby holes, while also adding positive charges to compensate the relatively excessive negative charges in diagonal directions. For the indentations, the charge deficits in horizontal and vertical directions are compensated by more concentrated positive charge in diagonal directions, in line with predictions in Section 4.3.3.

Though the compensating effect is visible from the figure for correction by walls and indentations, the difference for semicircular holes appears more subtle. This is due to the fact the correction by semicircular holes requires a modification accuracy smaller than 4 nm for eliminating the octupole effect. Though the difference between a round and a semicircular hole is hardly visible due to the 0.37 µm modification being small compared to the hole diameter of 15 µm, the octupole is fully eliminated. With a tolerance of 10 nm, the semicircular holes are also the most sensitive to construction defects. With a tolerance of 80 nm, the indentations are the least sensitive to errors, even considering the nonlinear behavior of the curve. However, the assumption for this geometry is a perfectly round aperture, whereas any physical round aperture will probably also have small defects that could cause field effects similar to the fields near the semicircular apertures.

Having obtained these optimal geometries, the different correction methods are compared by tracing particles through the central and the first off-axis aperture. The difference in the spots and thus the effect of these different correction methods is compared by measuring the FW_{50} in the focal planes. For a beamlet through the central aperture, the Full-Width-50 is denoted as $FW_{50,0}$ and for a beamlet through the first off-axis aperture the Full-Width-50 is denoted as $FW_{50,1}$. Table 2 summarizes these values for a single hole, a regular 5x5 aperture array and all optimized correcting geometries. The table also includes

the correction parameters and the fitted A1r astigmatism coefficient. The A1r coefficient is included here because there seems to be a significantly contributing factor in the difference between the spot sizes of the different corrected geometries: the lowest A1r term is attributed to octupole correction through aperture walls, resulting in the smallest $FW_{50,1}$ and the lowest A1r term is attributed to indentations, resulting in the largest $FW_{50,1}$ (excluding the uncorrected regular 5x5 grid).

From checking the particle distributions, it becomes clear that indeed the A1r term becomes a major aberration after correcting the octupole. This is demonstrated in Figure 30, where the electrons are scattered in two different z-positions, just before and just after focus for the simulation done with the geometry optimized with aperture walls and the geometry optimized with indentations. The horizontal and vertical scale is the same scale in all figures (1:1). For the geometry with walls (figures a and c), the spots look perfectly round, and thus the astigmatism term appears to be insignificant. For the geometry with indentations, the spot at $z = 0.03$ m (before focus) looks more spread out horizontally than vertically, and the opposite is happening at $z = 0.034$ m. This indicates a different focal plane horizontally and vertically, leading to a larger spot overall. Due to the A1r aberration, the correction through indentations leads to the largest spot. In fact, when comparing spot sizes, it turns out that an indentation of 7.809 µm (the result of the first iteration) in diameter leads to a smaller spot with $\mathrm{FW}_{50,1}$ = 0.64 µm, compared to $\mathrm{FW}_{50,1}$ = 0.67 µm for a geometry without an octupole contribution. This indicates that A1r becomes very dominant for the given corrections.

Though the indentations lead to a larger spot here, the construction tolerance is lowest and the A1r contribution might be correctable (discussed in section 5.4), which makes the indentations a viable option to reduce the spot size by eliminating the octupole contribution. However, for the given geometry, the correction through aperture walls leads to a relatively low A1r term and thereby also results in the smallest spot. Though semicircular holes lead to a relatively low A1r contribution, the central spot is larger (in $\mathrm{FW}_{50,0}$) compared to geometries with walls and indentations. Moreover, the construction tolerance of the semicircular holes is lowest, making this the least promising method to correct the octupole contribution. The 16-pole visible in Figure 20 for a different geometry is not visible in the spot for semicircular apertures here (hence not shown), but the effect might be playing a role in enlarging the spot.

Table 2: The Full-Width-50 (FW_{50}) results of beamlets through all central corrected aperture holes and the first off-axis hole. The FW_{50} for a single hole and a regular 5x5 grid are added for comparison. The parameter values and FW_{50} are displayed in µm.

Correction shape	*Parameter Value* (µm)	$\boldsymbol{FW_{50,0}}$(µm)	$\boldsymbol{FW_{50,1}}$(µm)	***A1r (m)***
Single hole	-	0.54	-	-
5x5 grid regular	-	0.96	0.98	-1.66e-4
Walls	0.88	0.54	0.53	-1.65e-5
Indentations	7.87	0.54	0.67	-2.30e-4
Semi-circular	0.37	0.56	0.61	-1.58e-4
Hexagonal regular	-	0.56	0.59	-9.33e-5
Hexagonal walls	0.66	0.54	0.54	-4.01e-5

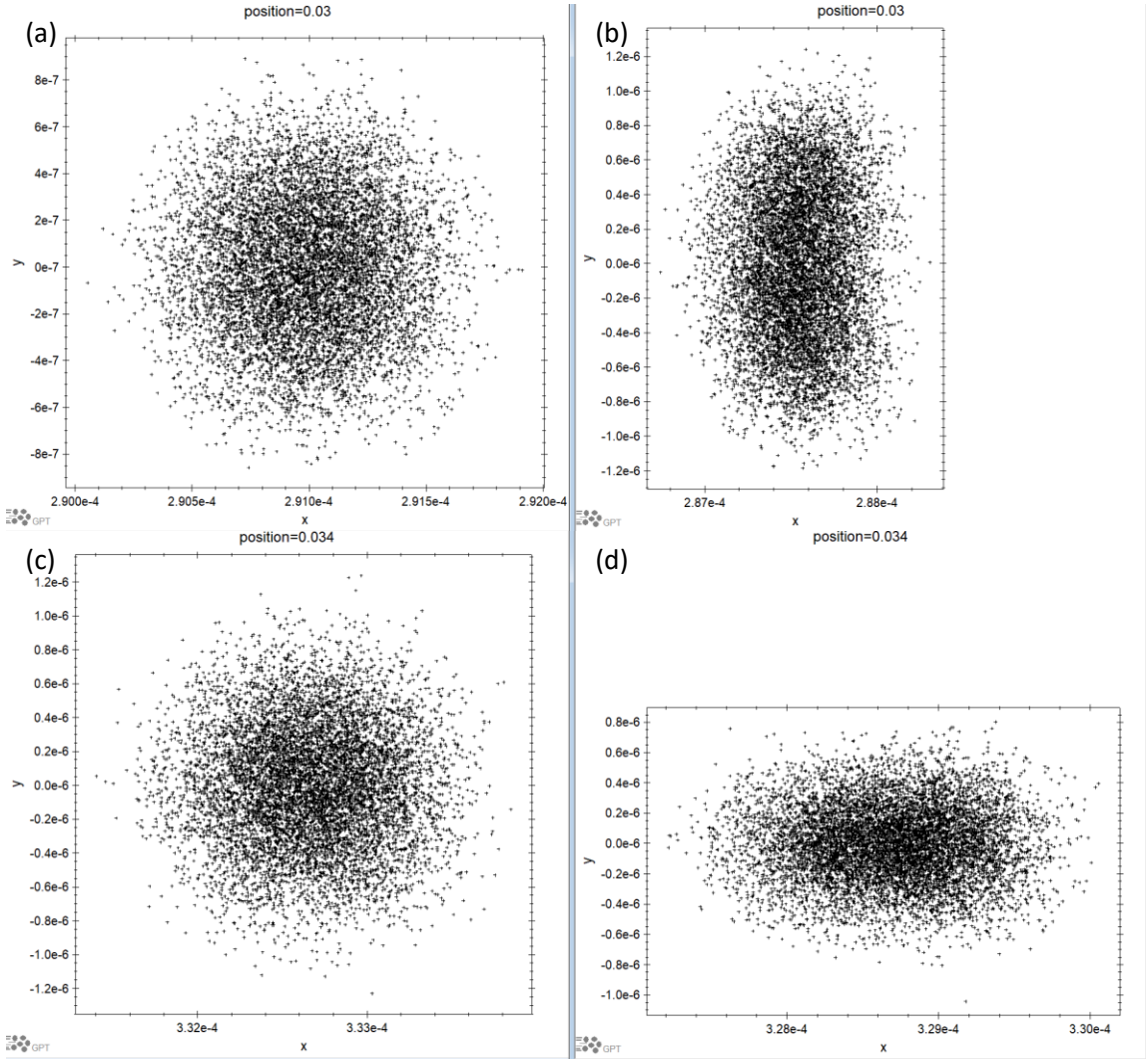

Figure 30: Spots for the ALA's corrected by aperture walls (Figures a and c) and by indentations (Figures b and d) for two different z-positions, indicated at the top of each figure. All values displayed are in m.

5.3 Multipole field expansion

When fitting the particle position aberrations, as described in section 2.6, for the optimized geometries aimed at eliminating the octupole aberrations, the calculated octupole aberration coefficient is either nullified or negligibly small. Another method to compare the effective removal of the octupole aberration from the field is by using the fitting procedure described in section 0, where the multipole field expansions are fitted. In Figure 31, $\phi_4[\mathrm{Vm}^{-4}]$ along the z-axis[µm] is plotted for a single aperture lens, the regular 5x5 grid and all square grid correction shapes. The octupole field for the single hole is shown to indicate the residual octupole field from the iterative charge BEMsolver. The vertical black lines indicate the front and back of the aperture plate (excluding aperture walls).

For a regular 5x5 grid, the multipole is mostly induced in front of the aperture plate. The three correction methods eliminate the effective multipole in different ways. For semicircular holes, this octupole field is equally strong before the aperture, but then corrected within the boundary of the aperture plate. The aperture walls and indentations seem to correct in a more stable manner by first lowering the initial

octupole field and then correcting the already lowered aberration contribution. The walls around apertures and indentations seem to work similarly, except for the fact that the potential aberration of the aperture lens with wall seems to be shifted slightly to a lower z-coordinate. This may be due to the wall protrusion effectively shifting the aperture lens by the height of the wall around it. This is a potential reason for the difference in the A1r term resulting from the simulations.

Integrating the potential aberrations to obtain $P_n = \int \phi_n(z)dz$ gives a value of -9.81e16 Vm^{-3} for the regular grid, and 7e14 Vm^{-3} for the single hole. This is acceptably low given that e.g. also the chamfering of aperture edges produces aberrations of this scale, and thus this contribution can be considered zero. Similarly, the values for the corrected ALA's are -3e14, -6e14 and -6e14 Vm^{-3} for aperture walls, indentations and semicircular holes respectively, which all add up to a lower field aberration than the octupole field aberration for a single aperture and can thus be considered zero as well. Therefore, the approach chosen in section 0 would have sufficiently got rid of the octupole for a central hole. However, this does not allow a comparison of the second largest aberration for off-axis apertures, which is the A_1 astigmatism contribution.

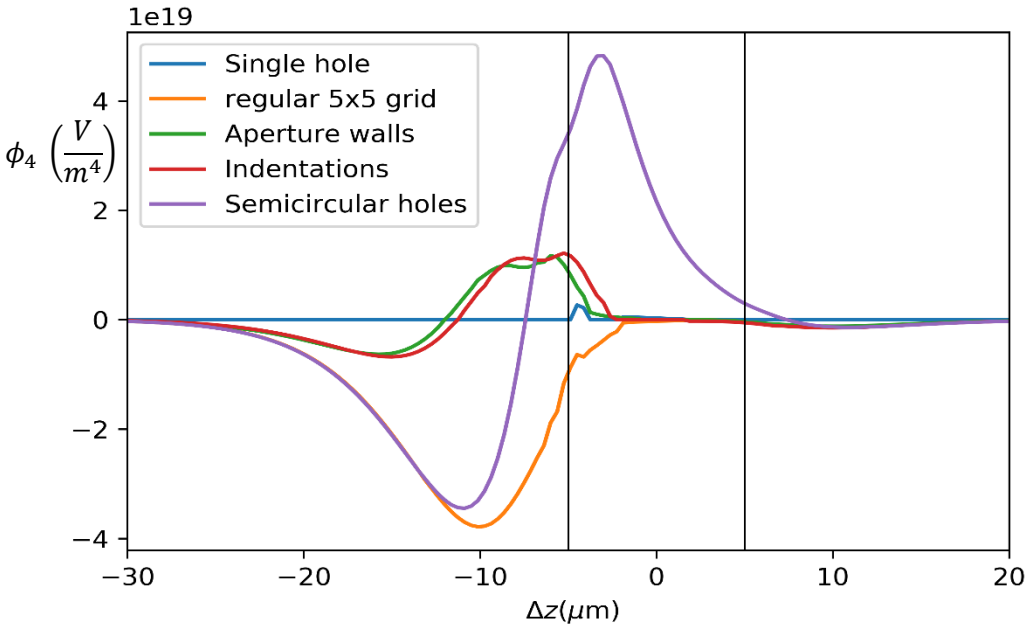

Figure 31: ϕ_4 potential aberration in Vm^{-4} for the single hole given along the z-axis in μm (now with $\Delta z = 0$ at the center of the ALA), the regular 5x5 grid and all square grid correction shapes. The octupole field for the single hole is shown to indicate the residual octupole field from the iterative charge BEMsolver. The vertical black lines indicate the front and back of the aperture plate (excluding aperture walls).

5.4 Two-fold astigmatism caused by nearby holes

As pointed out in section 4, the geometry of the MBS and the voltages have been optimized such that the contribution from geometrical off-axial aberrations, especially from (two-fold) astigmatism, A_1, is significantly suppressed. This optimization to eliminate the off-axial aberrations has been done by A. Mohammadi-Gheidari et al [9], where the rotationally symmetric fields calculated for a single central aperture are assumed to be valid when translated to the off-axis aperture locations to approximate the fields of a single aperture that is physically positioned off-axis. This approximation is only valid to a given

limit. As seen for the aberration fitting result for a regular 5x5 aperture array, there is a significant A1r contribution here. Though the effect is only minor for a regular 5x5 array compared to the more dominant octupole aberration and for the wall-corrected ALA in the first off-axis spot, one might wonder what will happen to further off-axis spots.

For that reason, another few further test cases are designed. The first being a check of the corrected astigmatism term in a geometry where only a single hole is displaced by 20 µm (which is equal to the pitch for the ALA). Indeed, we find an A1r term of only 4.75e-6 m, compared to -1.66e-4 m for an aperture array (also, there is no spot enlargement compared to an ALA with a single central aperture). This means that the addition of other apertures do play a role in spot enlargement, through an increased astigmatism term.

Another step is taken by comparing the aberrations for a single aperture hole that is displaced by 200 µm, to a geometry with a 3x3 grid of holes with a pitch of 200 µm where particles are traced through one of the off-axis holes. Both lead to some astigmatism, with A1r = -1.08e-5 m, for the single hole, and A1r = 2.15e-05 m for the 3x3 grid. In both cases, the octupole term is negligible, but despite this the field seems to be modified enough for problems to arise. Given that the value for A1r seems to be going up for an increasing number of holes in the plate, one might expect that this trend continues for more holes. When attempting to add more holes around the target hole by creating a 5x5 array (with pitch 100 um), the resulting astigmatism goes down again to A1r = -1.34e-05 m. This indicates that more work may be required to explore the effect. However, the study of only a 5x5 grid shows that the astigmatism resulting from the field modification by nearby holes may somewhat be compensated by adding walls around apertures. The extend of the applicability of this measure for further off-axis apertures is yet unknown and requires more study.

Because of the A1r contributions near the apertures, one could try altering the shapes and voltages for this geometry to get rid of the effect. For now, it appears that the aperture walls correct the effect considerably as well, making it a better option than indentations, assuming the desired construction tolerance of 30 nm can be achieved by MEMS technology.

6 Conclusion

The aperture lens array that splits the emission cone of the electron source into multiple beamlets, introduces an octupole aberration in these beamlets through the electrostatic interaction of nearby apertures. The practical quantification, and elimination of the octupole aberrations in this application is not commonly practiced. In this thesis, the method of tracing particles through the whole multi beam source, and fitting all (multipole) aberrations by mapping the position and momentum of the electrons from object plane to the image plane, a procedure that is now incorporated in GPT, is used to quantify the aberration coefficients. In order to eliminate the multipole induced by small cylindrically asymmetric structures, several approaches are discussed. It turns out that instead of fitting aberrations to traced particles, the more quickly calculated integrated electric field aberrations could have sufficed for correcting the octupole to within the tolerances used here.

Several correction methods, namely aperture walls, indentations, semicircular holes and a hexagonal aperture pattern (with and without aperture walls) have been applied to correct the octupole. All these methods eliminate the octupole for particles through the central aperture. However, there is a difference in parameter sensitivity for different methods in the multipole correcting shapes. Besides demonstrating

(dis)advantages between different types of solutions, this sensitivity also demonstrates the required precision to certain aspects of the ALA construction process.

For off-axis apertures, there are differences between the astigmatism, or effective quadrupole aberration, observed in the spot. The aperture walls seem to best preserve the behavior of the fields optimized for a single off-axis hole without astigmatism. For this reason, it is currently assumed to be the best correction method for this application, for which the desired construction sensitivity can also be achieved. The optimized indentations result in higher astigmatism and because of that the largest off-axial spot. This is an effect that can be studied more detail for the MBS in the future, and may be eliminated at some point. Semicircular apertures are less favorable due to their highly demanding construction accuracy and the less effective central spot size reduction, but also due to the suboptimal off-axis beam aberrations involved.

7 References

[1] ASML Holding, "TWINSCAN NXE:3400B," [Online]. Available: www.asml.com/en/products/euv-lithography-systems/twinscan-nxe3400b. [Accessed 18 August 2020].

[2] "Life through a Lens," NobelPrize.org, [Online]. Available: www.nobelprize.org/prizes/physics/1986/perspectives. [Accessed 18 August 2020].

[3] HyperPhysics, "DeBroglie Wavelength," [Online]. Available: http://hyperphysics.phy-astr.gsu.edu/hbase/debrog.html#c1. [Accessed 18 August 2020].

[4] Thermo Fisher Scientific, "Spectra 300 S/TEM for," [Online]. Available: assets.thermofisher.com/TFS-Assets/MSD/Datasheets/Spectra-300-semiconductors-datasheet.pdf. [Accessed 18 August 2020].

[5] P. Hawkes and E. Kasper, Principles of Electron Optics, Academic press, 1996.

[6] Thermo Fisher Scientific, "Quattro," [Online]. Available: assets.thermofisher.com/TFS-Assets/MSD/Datasheets/Quattro-datasheet.pdf. [Accessed 18 August 2020].

[7] A. Mohammadi-Gheidari, 196 Beams in a Scanning Electron Microscope, PhD thesis, Delft, University of Technology, 2013.

[8] B. J. G. M. &. B. J. E. Roelofs, " Feasibility of multi-beam electron lithography," *Microelectronic engineering,* vol. 2, no. 4, pp. 259-279, 1984.

[9] A. Mohammadi-Gheidari, E. Kieft, X. Guo, M. Wisse, M. Kamerbeek and P. Kruit, "to be published".

[10] Pulsar Physics, "General Particle Tracer," 1996. [Online]. Available: http://www.pulsar.nl/.

[11] J. Orloff, Handbook of Charged Particle Optics, Boca Raton: CRC Press, 2008.

[12] J. D. Jackson, Classical electrodynamics, John Wiley & Sons, 2007.

[13] A. Alvin and M. Schimek, Methods of multivariate analysis, New York: John Wiley & Sons, Inc, 1997.

[14] Y. Liao, "Practical Electron Microscopy and Database," 2018. [Online]. Available: www.globalsino.com/EM/. [Accessed 8 7 2020].

[15] D. Typke and K. Dierksen, "Determination of image aberrations in high-resolution electron microscopy using diffractogram and cross-correlation methods," *Optik,* vol. 99, no. 4, pp. 155-166, 1995.

[16] H. A. Van der Vorst, "Bi-CGSTAB: A fast and smoothly converging variant of Bi-CG for the solution of nonsymmetric linear systems.," *SIAM Journal on scientific and Statistical Computing,* vol. 13, no. 2, pp. 631-644, 1992.

[17] A. Mohammadi-Gheidari, T. Radlicka, X. Guo and P. Kruit, ""to be published"".

[18] M. S. Bronsgeest, Physics of Schottky Electron Sources, Phd Thesis, Delft, 2009.

[19] H. Liu, E. Munro, J. Rouse and X. Zhu, "Simulation methods for multipole imaging systems and aberration correctors," *Ultramicroscopy,* vol. 93, no. 3-4, pp. 271-291, 2003.

[20] M. Born and E. Wolf, Principles of Optics, New York: Pergatnon, 1980.

[21] R. Knippelmeyer, O. Kienzle, T. Kemen, H. Mueller, S. Uhlemann, M. Haider, A. Casares and S. Rogers, "Particle-Optical Systems and Arrangements and Particle-Optical Components for such Systems and Arrangements". United States Patent 20140158902, 12 June 2014.

[22] J. Ahrens, B. Geveci and C. Law, ParaView: An End-User Tool for Large Data Visualization, Elsevier, 2005.

8 Acknowledgement

I would like to thank Dr. Ali Mohammadi-Gheidari, my daily supervisor first for making my graduation project at Thermo Fisher possible at all, my discussions with him that helped get the project going and getting it finished, and for the pleasant coffee/lunch-break discussions. At Thermo Fisher, Dr. Erik Kieft also helped me a great deal when I was facing problems getting GPT to work on a remote Linux server. Other colleagues that made my project possible are Tor Halsan for more complicated problems on the server, Dr. Sander Henstra and Dr. Peter Tiemeijer for the discussions we had and of course Dr. Luigi Mele who, as my manager, showed great interest in my progress and was responsible for getting the administrative work to work! Finally, Dr. Bart Buijsse and many other colleagues at Thermo Fisher who welcomed me to their club but also showed interest in my project. I would like to thank Thermo Fisher people for their hospitality.

Outside Thermo Fisher, I would like to thank Pulsar Physics for helping me with the technical effort of BEM+GPT software and especially getting the fitting procedure to produce results, and finally Dr. Peter Mutsaers for being my supervisor from TU/e and helping me by discussing progress along the way.